Tectono-metamorphic evolution of UHP Zermatt-Saas serpentinites: a tool for vertical palaeogeographic restoration

Journal:	*International Geology Review*
Manuscript ID	TIGR-2019-0424.R1
Manuscript Type:	Data Article
Date Submitted by the Author:	n/a
Complete List of Authors:	Luoni, Pietro; Università degli Studi di Milano, Scienze della Terra Ardito Desio Rebay, Gisella; Università degli Studi di Pavia Roda, Manuel; Università degli Studi di Milano, Scienze della Terra Ardito Desio Zanoni, Davide; Università degli Studi di Milano, Scienze della Terra Ardito Desio Spalla, Maria Iole; Università degli Studi di Milano, Scienze della Terra Ardito Desio
Keywords:	Ti-humites, serpentinite, subduction modelling, Piemonte Zone, Western Alps

Tectono-metamorphic evolution of UHP Zermatt-Saas serpentinites: a tool for vertical palaeogeographic restoration

Pietro Luoni[a]*, Gisella Rebay[b], Manuel Roda[a], Davide Zanoni[a] and Maria Iole Spalla[a]

[a]*Dipartimento di Scienze della Terra 'A. Desio', Università degli Studi di Milano, Milano, Italy;*
[b]*Dipartimento di Scienze della Terra e dell'Ambiente, Università degli Studi di Pavia, Pavia, Italy*

*Dipartimento di Scienze della Terra 'A. Desio', Università degli Studi di Milano, Via Mangiagalli, 34 - 20133 Milano, Italy. pietro.luoni@unimi.it

Orcid ID:
Pietro Luoni: 0000-0001-9957-1388
Gisella Rebay: 0000-0001-8353-2683
Manuel Roda: 0000-0002-5446-6434
Davide Zanoni: 0000-0003-1404-4824
Maria Iole Spalla: 0000-0001-8346-5070

Tectono-metamorphic evolution of UHP Zermatt-Saas serpentinites: a tool for vertical palaeogeographic restoration

Within the Zermatt-Saas Zone (ZSZ, northwestern Alps), Ti-chondrodite- and Ti-clinohumite-bearing assemblages in serpentinites indicate UHP conditions. Multiscale structural analysis (1:20 scale mapping) and petrological investigation of serpentinites at Créton (upper Valtournanche) evidenced a polyphasic deformation and metamorphic history. In this locality and at regional scale, S2 is the dominant foliation that developed under HP-UHP conditions. Pre-D2 mineral and textural relicts are preserved despite the pervasiveness of S2. Pre-D2 olivine + Ti-chondrodite + spinel assemblage implies re-equilibration at 2.8–3.3 GPa and 600–630 °C, in agreement with conditions recorded by coesite- and microdiamond-bearing rocks in the Cignana Lake Unit. The PT conditions inferred for syn-D2 assemblages at Créton are similar to those estimated for D2 in the surrounding serpentinites, which were dated at 65 ± 5.6 Ma. These results suggest that portions of ZSZ were subducted at high depth before 70 Ma and widen the time span during which ZSZ recorded PT peak conditions. The comparison of these data with results of a numerical model of an ocean-continent subduction system gives insights on coupling stages of this UHP unit with the surrounding ZSZ rocks during the Alpine convergence and vertical palaeogeography during different time steps.

Keywords: Ti-humites, serpentinite, subduction modelling, Piemonte Zone, Western Alps

1. Introduction

Emplacement of Ultra High Pressure (UHP) rocks in the axial portion of orogenic chains (Chopin 1984; Smith 1984; Kienast *et al.* 1991; Reinecke 1991; Ernst and Liou 1999) has opened up the need to identify the geodynamic context of their formation and coupling with the surrounding units, apparently free of this metamorphic imprint, and precisely if such formation and/or coupling occurred in a context of subduction, collision or, even, of late orogenic extension. Moreover, the discussion on exhumation mechanisms and timing that are effective for the preservation of UHP assemblages is still open. In the Alps the detection of UHP mineral phases, such as coesite, ellenbergerite, Mg-dumortierite, and microdiamonds, allowed the individuation of hectometre- to kilometre-scale UHP tectonic units enclosed in HP nappes both of oceanic (Zermatt-

Saas Zone) and continental (Dora Maira Massif) origin (e.g. Chopin 1984; Chopin *et al.* 1986; Reinecke 1991; Ferraris *et al.* 1995; Frezzotti *et al.* 2011). In the last decades several UHP mineral records have been detected in metabasites and metasediments of the Zermatt-Saas Zone (Reinecke 1991; Reinecke *et al.* 1994; van der Klauw *et al.* 1997; Bucher *et al.* 2005; Groppo *et al.* 2009; Frezzotti *et al.* 2011) and more recently UHP conditions have been reported also in serpentinites from Créton, in upper Valtournanche (Luoni *et al.* 2018). In particular, the hectometre-sized Cignana Lake Unit and the UHP Créton serpentinites are localised close to the tectonic contact between Zermatt-Saas and Combin zones (Forster *et al.* 2004; Luoni *et al.* 2019 and refs. therein). As evidenced by reviewing the rich-literature (Rebay *et al.* 2018 and refs. therein), the inferred P_{max} conditions are heterogeneous and the proposed metamorphic evolutions are not coherent and often contrasting, as well as the peak radiometric ages , which are spread over a time interval from Upper Cretaceous to middle Eocene.

Therefore, a comparison between high-detailed structural and metamorphic data, defining the tectono-thermal evolution of these UHP slices, with the predictions from quantitative geodynamic models becomes a fundamental key to investigate their potential formation and coupling environment during different stages of the convergent Alpine history.

With this aim, this contribution shows a multiscale structural and petrological analysis that is finalised to define the P-T-d-t evolution of the Créton UHP serpentinites. The results are compared with the prediction of a 2D quantitative geodynamic model of an ocean-continent subduction system.

2. Geological setting

The Zermatt-Saas Zone (ZSZ) is one of the main units of the Piemonte Zone in the Penninic domain of the Western Alps (Figure 1a; Bigi *et al.* 1990; Dal Piaz 1992; Dal Piaz 2010; Balestro *et al.* 2019 and references therein). The Piemonte Zone occurs in the axial part of the Western Alps, from the Ligurian Alps to Switzerland (Figure 1a) and is bordered by the Sesia-Lanzo Zone and the Po Plain to the east, and the Briançonnaise Zone to the west (Beltrando *et al.* 2010; Dal Piaz 2010; Spalla *et al.* 2010; Roda *et al.* 2019 and references therein). It mostly comprises meta-ophiolites consisting of serpentinites, metagabbros, metabasites, and metasediments with minor continental outliers (Fassmer *et al.* 2016; Weber and Bucher 2015 and refs therein).

The ZSZ is interpreted as a remnant of the Alpine Tethys oceanic lithosphere, sutured in the Alpine belt during the Alpine subduction and collision (Dal Piaz 2001; Reddy *et al.* 1999; Balestro *et al.* 2019). Together with the Combin Zone (CZ), ZSZ is sandwiched between the continental nappes of Monte Rosa and Dent Blanche (Figure 1b). ZSZ and CZ are separated by the Pancherot-Cime Bianche-Bettaforca unit (PCB). The CZ is characterised mostly by metasedimentary rocks with minor metabasalts, metagabbros, and serpentinites and interpreted as derived from an ocean-continent transition zone (e.g. Dal Piaz and Ernst 1978; Dal Piaz *et al.* 1981). CZ rocks recorded blueschist facies conditions during the Alpine convergence, recognizable despite the pervasive greenschist facies metamorphism (Reddy *et al.* 1999; Bousquet *et al.* 2004 and reference therein). Laying between ZSZ and CZ, PCB is a discontinuous horizon of metasedimentary rocks of Austroalpine affinity, dominated by greenschist facies metamorphic imprint, whose protoliths are thought to be deposited on a thinned continental margin (Dal Piaz 1988; Dal Piaz 1999; Passeri *et al.* 2018).

The ZSZ preserves a complete ophiolitic sequence derived from the internal portion of the oceanic realm (Bearth 1967; Ernst and Dal Piaz 1978; Martin *et al.* 1994; Tartarotti *et al.* 2017). It includes serpentinites (Li *et al.* 2004a; Rebay *et al.* 2012), metagabbros and metarodingites (Li *et al.* 2004b; Zanoni *et al.* 2016), metabasites (Bucher *et al.* 2005 and reference therein), and metasedimentary cover, which consists of calcschists, marbles, and quartzites. Ophiolites locally enclose continental slices, such as the Theodul Glacier Unit (TGU) (Weber and Bucher 2015). The age of protoliths is proposed to be 164-153 Ma for metagabbros and metabasites (Rubatto *et al.*

1998) in the Swiss portion of ZSZ, and 168-162 Ma for basalt melt-percolated serpentinites in Valtournanche (Rebay *et al.* 2018). The whole ZSZ is dominated by an eclogite facies metamorphic imprint, registered during the Alpine subduction, and overprinted by epidote amphibolite and greenschist facies metamorphism (Ernst and Dal Piaz 1978; Spalla *et al.* 1996; Rebay *et al.* 2012; Rebay *et al.* 2018). Since Reinecke (1991) inferred metamorphic PT peak conditions of 2.6-2.8 GPa and 590-630 °C for quartzites in the Cignana Lake Unit (CLU; Figure 1b and Figure 1c), HP-UHP peak conditions have been estimated in other localities of the ZSZ. Metabasites of Saas-Fee experienced PT conditions from 1.9-2.2 GPa and 530-600 °C (Dale *et al.* 2009) and 2.3-2.5 GPa and 530-555 °C (Angiboust *et al.* 2009) to 2.5-3.0 GPa and 550-600 °C (Bucher *et al.* 2005). Metagabbros in the Swiss portion of ZSZ registered peak conditions of 1.75-2.0 GPa and 550-600 °C (Barnicoat and Fry 1986), 2.5 GPa and 650 °C (Meyer 1983) and 2.5 GPa and 610 °C (Bucher and Grapes 2009). Further estimates in CLU show PT conditions from 2.7 to over 3.2 GPa and temperatures of 590-630°C (van der Klauw *et al.* 1997; Reinecke 1998; Groppo *et al.* 2009), accompanied by the discovery of microdiamonds in oceanic metasediments (Frezzotti *et al.* 2011). HP-UHP peak conditions are also reported for the mantle rocks of the ZSZ: serpentinites from the Swiss portion of the ZSZ recorded peak conditions at 2.0-2.5 GPa and 600-650 °C (Li *et al.* 2004a) while serpentinites from Valtournanche experienced peak conditions at 2.2-2.8 GPa and 580-620 °C (Rebay *et al.* 2012), together with the associated rodingites at 2.3-2.8 GPa and 580-660 °C (Zanoni *et al.* 2016). In TGU at Trockener Steg (Zermatt area) peak conditions of 2.2-2.3 GPa and 515-645 °C are estimated in a continental slice enclosed within ZSZ (Weber and Bucher 2015).

ZSZ serpentinites have been interpreted to be affected by an ocean floor metasomatism responsible for serpentinisation of the peridotites and rodingitisation of the associated gabbroic dikes (Rahn and Bucher 1998; Li *et al.* 2004b; Zanoni *et al.* 2016). Ti-clinohumite in veins and aggregates has been interpreted as the record of both ocean-floor metasomatism, at conditions of 0.4 GPa and 420 °C (Rahn and Bucher, 1998), and HP-UHP syn-subduction metamorphism, since Ti-clinohumite is in textural equilibrium with HP mineral assemblages (Scambelluri and Rampone 1999; Groppo and Compagnoni 2007; Ferrando *et al.* 2010; Rebay *et al.* 2012).

Recently at Créton (see Figure 1d), the finding of Ti-chondrodite and Ti-chondrodite + Ti-clinohumite bearing assemblages allowed inferring UHP conditions predating the HP-UHP regional fabrics in the ZSZ serpentinites (Luoni *et al.* 2018). Soon after, Ti-chondrodite was also found in CLU serpentinites (Gilio *et al.* 2019).

Although all these peak PT estimates disclose HP-UHP conditions, differences in P and T values occur (see Rebay *et al.* 2018), together with a heterogeneous areal distribution of P_{max} conditions. Furthermore, peak ages range between 68 and 38 Ma, although evidence of prograde metamorphism dates back at 80 Ma (e.g. Skora *et al.* 2015). These data (Table 1) are in contrast with ZSZ experiencing a homogeneous evolution during the Alpine convergence (e.g. Angiboust *et al.* 2009; Angiboust and Agard 2010), but rather enforce the interpretation of a heterogeneous metamorphic evolution covering a wide time span during the subduction of the ZSZ rocks and associated continental slivers (Spalla *et al.* 1996; Gerya and Stöckhert 2005; Spalla *et al.* 2010; Roda *et al.* 2012).

3. Deformation history

Valtournanche serpentinites and rodingites underwent a common structural evolution of three ductile syn-metamorphic stages (D1, D2, D3) followed by a stage (D4) not associated with new mineral growth (Rebay *et al.* 2012; Zanoni *et al.* 2012). During D2 the most pervasive foliation S2 developed under HP conditions (Figure 1d). D3 structures consist of open folds and the associated S3 foliation, whereas D4 mostly consists of open folds with sub vertical axial planes. Créton outcrops have been the subject of high-precision structural mapping at 1:20 scale to further investigate pre-D2 evolution and to precisely define the rich lithostratigraphy of UHP serpentinites (Figure 2, Luoni *et al.* 2019).

Créton serpentinites are close to the boundary with calcschists and metabasites of the CZ (Figure 1d). They contain layers of magnetite and embed rare decimetre-thick pyroxenite and olivine-rich layers and lenses. Locally Ti-chondrodite and Ti-clinohumite and olivine veins occur. The effects of polyphasic deformation, which affects the original lithostratigraphy, are synthesised in Figure 3.

As described by Luoni *et al.* (2019), D1 structures are rare D1 rootless fold hinges marked by magnetite layers, olivine-rich layers, Ti-chondrodite + Ti-clinohumite veins (Figure 3a), and S1 foliation in an olivine-rich lens.

D2 produced tight to isoclinal folds of olivine-rich layers (Figure 3b) and boudins of olivine-rich layers, pyroxenite, and Ti-chondrodite + Ti-clinohumite veins, locally with a granoblastic texture in which an oriented fabric is lacking. Magnetite layers are often asymmetrically crenulated by D2. S2 is a mylonitic, locally composite, foliation (Figure 3b) and represents the dominant structure. S2 shows a dip azimuth at W-WNW/14°- 65° and is observed in all lithotypes intersecting previous structures.

Rare D3 centimetre-wide crenulation affects S2 in serpentinites. D3 fold axial planes dip WNW with medium angle and fold axes dip at a low angle towards WSW (Luoni *et al.* 2019). S3 axial plane foliation has been recognised only at the microscale. D3 also developed shear zones deflecting S2, magnetite layers (Figure 3c) and olivine-rich layers.

4. Syn-metamorphic fabric evolution

Petrographic and structural microanalysis is focused on serpentinites and embedded rocks such as olivine-rich layers and lenses, pyroxenites, and Ti-chondrodite + Ti-clinohumite veins. S2 affects serpentinites and all the embedded lithotypes and contains pre-D2 mineral and textural relicts consisting of S1 relics or deformed veins and lenses with granoblastic textures. Because D2 fabrics dominate, porphyroclasts, lenticular aggregates of polygonal grains, and S1 marking rootless fold hinges wrapped by S2 (in places mylonitic), are labelled as pre-D2 relics, since univocal chronological relationships between porphyroclasts and mineral aggregates, and S1 structures are not preserved.

Four subsequent mineral assemblages were distinguished (Table 2): *pre-D2* relics are different types of porphyroclasts and mineral aggregates wrapped by S2, locally marking S1 foliation; *pre-D2-to-early-D2* minerals constitute polygonal aggregates, often around pre-D2 porphyroclasts, and are wrapped by S2. *D2* assemblages underline S2 foliation and fill syn-D2 boudins necks. Locally syn-D3 minerals overgrew S2 foliation or marked incipient D3 folds axial plane foliation. Mineral abbreviations are from Whitney and Evans (2010).

4.1 Serpentinite

Antigorite marks both pre-D2 and syn-D2 domains. SPO (shape preferred orientation) of Atg2 flakes defines S2 mylonitic foliation with Mag2 and Ol2 (Figure 4a) or Cpx2 (Figure 4b). Often Cpx2 is parallel to Chl2 SPO and LPO (Figure 4b). S2 wraps pre-D2 centimetre-sized oval aggregates of antigorite: they can be constituted of oriented fibres of Atg or made of interlobate Atg lamellae in mesh textures. Submillimetre-sized pre-D2 olivine porphyroclasts are wrapped by S2 and often enclose sharp-edged and anhedral to rounded Mag (Figure 4a). Furthermore, pre-D2 Ol aligned porphyroclasts constitute the remnants of olivine veinlets. Pre-D2 Ol shows undulose extinction, and contains Ti-Chu lamellae, Atg, Mag, and fluid inclusions. Ol2 often rims pre-D2 Ol. Locally, Cpx2 or Ol2 and Atg2 occur in S2 pressure shadows of pre-D2 Ol. Pre-D2 millimetre-sized rounded Cr-Mag and Mag are wrapped by S2 and often rimmed by Mag2. Mag2 grains are aligned in submillimetre layers along S2 (Figure 4a). Chlorite constitutes lenses and anastomosed layers wrapping Cpx2 aggregates and Ti-chondrodite + Ti-clinohumite veins. Aggregates of chlorite contain Chl2 grains parallel to S2, locally rimmed by Chl3. Locally, in Chl-rich aggregates, S2 is marked by Chl2 ± Atg2 and wraps pre-D2 Chl porphyroclasts as they display different LPO with respect to minerals underlying S2. Pre-D2 Ti-Chu porphyroclasts with undulose extinction are scattered in the serpentinite matrix and are wrapped by S2 foliation marked by Atg2 + Mag2 ± Ti-Chu2. SPO of Atg3 and Mag3 marks the rare S3 foliation and D3 shear zones with Amph3. Rare dolomite porphyroclasts are wrapped by S2 marked by Dol2 + Mag2 + Atg2 + Ol2. Up to millimetre-sized rare apatite porphyroclasts, with undulose extinction are wrapped by S2 defined by Atg2 + Cpx2 + Chl2. Calcite veins are locally parallel to S2 foliations (Cal2) and fill fractures crosscutting S2 (post-D2 Cal).

4.2 Olivine-rich layers and lenses

Olivine-rich layers display massive cores with more than 90% of olivine and strongly foliated rims with a higher modal amount of Atg than the cores. The cores of these layers contain millimetre pre-D2 subhedral Ol porphyroclasts (Figure 4c) with weak undulose extinction and fractures. Locally their SPO is parallel to the S2 foliation wrapping or crosscutting the layers. They are rich in inclusions of micron-sized Mag and Atg. Mag is mostly sharp-edged and rounded while Atg flakes may have both sharp and irregular edges. Ol porphyroclasts are surrounded by polygonal aggregates of submillimetre pre-D2-to-early-D2 Ol + Atg + Mag. These aggregates do not show any preferred orientation. Edges between grains are sharp and Mag inclusions are common. Mag is also interstitial among Ol polygonal grains. Micron-sized, rounded, and sharp-edged inclusions of clinopyroxene occur both in pre-D2 and in pre-D2-to-early-D2 Ol. In the rims of the layers, where S2 is pervasive, Atg is more abundant than Ol and wraps pre-D2 Ol porphyroclasts. Polygonal pre-D2-to-early-D2 Ol occurs in pressure shadows of pre-D2 Ol, whereas Ol2 is very fine grained and shows SPO parallel to the foliation marked by Atg2 + Ol2 + Mag2. Ol2 with Atg2 also fill syn-D2 necks of pre-D2 Ol boudins. Locally, Mag2 and Chl2 rim pre-D2 Cr-Mag porphyroclasts. An olivine-rich lens is foliated and banded with alternating layers respectively richer in Ol and Atg. In the millimetre Ol-rich layers pre-D2 Ol relicts are anhedral, fractured, and display slight undulose extinction. They are partially surrounded by polygonal aggregates of submillimetre-sized Ol. Both the porphyroclasts and the polygonal aggregates are contained in a micron-sized matrix of polygonal Atg + Ol + Mag, with Pre-D2 Cr-Mag porphyroclasts rimmed by Mag and Fe-Chl.

4.3 Pyroxenite

Anhedral to subhedral centimetre-sized pre-D2 Cpx porphyroclasts are strongly deformed, locally kinked, with exsolution of Ilm + Mag (Figure 4d) and contain Atg + Chl + Ti-Chn and Ti-Chu along cleavages. Locally rare exsolutions- and strain-free augite cores are preserved in pre-D2 Cpx crystals.

Cpx porphyroclasts are often partially or totally replaced by Cpx2 new grains and Chl2. S2 oriented aggregates of Atg2 + Chl2 + Mag2 + Cpx2 wrap Cpx porphyroclasts where Chl2 and Atg2 SPO is parallel to S2. Locally, between the rim of Cpx porphyroclasts and millimetre globular aggregates of Ilm + Mag (former Spl), aggregates of polygonal pre-D2-to-early-D2 Ti-Chn + Ti-Chu occur (Figure 4e). The grain boundaries among Ti-humites, Ilm, and Mag are sharp and those between Ti-humites and Cpx porphyroclasts are interdigitated; locally Ti-humites occur along Cpx porphyroclasts cleavages.

4.4 Ti-Chu + Ti-Chn veins

Millimetre-sized pre-D2 Ti-Chn porphyroclasts are subhedral and twinned, with tapering lamellae, and enclose Atg and Mag (Figure 4f). Ti-Chn + Ti-Chu submillimetre subhedral grains constitute pre-D2-to-early-D2 assemblage together with Chl, Atg, Ilm, and Mag (Figure 5a and Figure 5b). Ol constitutes pre-D2 porphyroclasts locally replaced by pre-D2-to-early-D2 almost equigranular, subhedral Ol grains. Locally pre-D2-to-early-D2 Ol constitutes ribbon-shaped aggregates parallel to S2. Ol2 also marks S2 with SPO of submillimetre grains. Pre-D2 millimetre-sized and anhedral Spl is replaced by Ilm + Mag exsolutions (similarly to Figure 5c and Figure 5d). Pre-D2-to-early-D2 Ilm + Mag are often equigranular and with sharp edges in polygonal Ti-Chn + Ti-Chu aggregates.

5. Mineral compositional evolution

WDS mineral analyses were acquired from different microstructural sites by using the electron microprobe (JEOL 8200 Super Probe) operating at the “A. Desio” Earth Science Department of Milano University. A 15 keV accelerating voltage and a beam current of 15nA were used. Natural silicates were used as standards and matrix corrections were calculated using the ZAF procedure. Mineral formulae were recalculated on the basis of the following number of oxygen atoms: 4 for olivine, 6 for clinopyroxene, 116 for serpentine (Padrón-Navarta *et al*. 2013), 28 for chlorite, 4 for magnetite, 3 for ilmenite, and 23 for amphibole. Ti-chondrodite and Ti-clinohumite formulae were recalculated on the basis of 7 and 13 cations, respectively. Fe^{3+} in ilmenite was recalculated according to Droop (1987). Diagrams showing the significant compositional variations of the main minerals are shown in Figure 6 and a synthesis of the mineral compositions is reported in Table 3.

Olivine in serpentinites and olivine-rich layers is fosteritic ($0.89 < X_{Mg} < 0.96$) and its composition is mainly influenced by bulk rock (Figure 6a): olivine from the olivine-veins in serpentinite is the richest in Mg and olivine within Ti-clinohumite and Ti-chondrodite porphyroclasts is the richest in Fe. Olivine from olivine-rich layers shows the highest variation of Mg and Fe content, with the exception of olivine marking the relic S1, which has intermediate values of Fe. Mn is lower than 0.01 a.p.f.u.. Al, determined by ICPMS, is in the range 0.33-3.59 ppm (Table 4).

Ti-chondrodite and Ti-clinohumite: Ti-chondrodite is higher in both M/Si and TiO_2 than Ti-clinohumite. Ti-clinohumite2 shows higher M/Si and TiO_2 than Ti-clinohumite in pre-D2-to-early-D2 polygonal grains. Similarly, pre-D2-to-early-D2 Ti-Chn has higher M/Si and TiO_2 than pre-D2 Ti-Chn porphyroclasts (Figure 6b).

Clinopyroxene: in olivine-rich layers and serpentinites, pre-D2 Cpx and Cpx2 have a diopsiditic composition (Morimoto, 1988; Figure 6c). Ca is generally comprised between 0.88 and

1.02 a.p.f.u., whereas Cr is < 0.06 a.p.f.u. and Ti and Al are lower than the detection limit (Table 3). In pyroxenites, Pre-D2 Cpx cores and pre-D2-to-early-D2 Cpx are augite, with pre-D2-to-early-D2 Cpx richer in Ca and Al (up to 1.5 a.p.f.u.). Cpx2 is a pure diopside. The Ca increase from pre-D2 to D2 is accompanied by a decrease of Al and Na. Ti is < 0.05 a.p.f.u. and Cr is < 0.04 a.p.f.u. in pre-D2 and pre-D2-to-early-D2 Cpx and they are lower than detection limit in Cpx2 (Table 3; Figure 6c).

Serpentine composition (Figure 6d) is mainly influenced by whole rock composition. Atg from Ti-Chn + Ti-Chu veins is the richest in Mg, whereas Atg from pyroxenites is the richest in Fe.

Oxides: Spinel (Ferracutti *et al.* 2015) is Mag and its composition varies as a function of microstructural sites and bulk rock composition (Figure 6e): in olivine-rich layers and lenses, cores of Mag porphyroclasts are richer in Cr than the rims, and Mag2 (i.e. the rims) is pure magnetite; in serpentinites and Ti-Chn + Ti-Chu veins, both pre-D2 Mag and Mag2 are pure magnetite; oxide exsolutions in clinopyroxene porphyroclasts consist of magnetite. Ilmenite has low Mn contents in all rock types (0.04-0.15 a.p.f.u.). In pyroxenite, ilmenite shows Mg in the range 0.33-0.57 a.p.f.u.; in serpentinite ilmenite has low Mg in symplectites (0.02-0.04 a.p.f.u.) and 0.40-0.43 a.p.f.u. in Ilm2; in Ti-Chn + Ti-Chu veins, Mg in pre-D2-to-early-D2 Ilm is usually 0.05-0.31 a.p.f.u., with higher values in polygonal aggregates. Ilm2 shows Mg between 0.26 and 0.31 a.p.f.u. in polygonal aggregates .

Chlorite is generally penninite (Deer *et al.* 1992) in all rock types and no appreciable differences have been recognised among different generations (Table 3) and lithotypes. Al content varies between 2.43 and 3.13 a.p.f.u. and X_{Mg} is between 0.91 and 0.94.

Syn-D3 *amphibole* in serpentinites is tremolite (Locock, 2014). X_{Mg} varies between 0.95 and 0.96, Ca varies between 1.73 and 1.96 a.p.f.u., Al is < 0.06 a.p.f.u., and Na < 0.07 a.p.f.u..

6. Physical conditions of metamorphism

Microstructural observations, considered the influence of deformation mechanisms on reaction progress in the different microstructural sites to better constrain PT estimates relative to superposed fabrics (e.g. Passchier *et al.* 1990; Spalla and Zucali 2004; Passchier and Trouw 2005; Vernon 2018), and in Créton serpentinites allowed distinguishing two subsequent parageneses (Table 2) that occur in domains wrapped by S2:

(a) pre-D2 Ti-Chn + Atg + Spl ± Chl + Ol/Cpx,

(b) pre-D2-to-early-D2 Ti-Chn + Ti-Chu + Atg + Ilm + Mag + Ol/Cpx.

On the contrary S2 is marked by the Ti-Chn-free assemblage:

Ti-Chu + Atg + Mag + Chl + Ol/Cpx.

Metamorphic reaction curves from the literature, for Ti-poor and Ti-rich systems (Shen *et al.* 2015) and pseudosections allow inferring the PT evolution of Créton rocks (Figure 7). In the Ti-rich system experiments, Ti-Chn-out is at higher P_{min} (2.6-3.0 GPa at 550-670 °C) than in the Ti-poor system (Figure 7a), which shows Ti-Chn + Ti-Chu stable together between 1.9 and 2.8 GPa (at 550-670 °C). Temperatures in our samples are constrained using the Al content in pre-D2 Ol porphyroclasts and pre-D2-to-early-D2 polygonal Ol (De Hoog *et al.* 2010), represented as green and blue lines considering a 2 σ error, respectively. T_{max} is limited by the Atg out curve at 670 °C in both systems.

D2 metamorphic conditions have been modelled in the CFMASHO system with pseudosections using version tc345 of THERMOCALC software (Holland and Powell 1998; Powell *et al.* 1998; dataset tc-ds62) for two different samples: in the first sample Cpx does not occur and S2 is marked by Ol + Atg + Mag, in the second sample Ol is not present and S2 is underlined by Cpx + Atg + Chl + Mag. The amphibole and pyroxene activity-composition models are those of Diener *et* *al.* (2007) and of Zeh *et al.* (2005), respectively. The garnet models are from White *et al.* (2007) (but with the garnet asymmetry involving αgr = 3 instead of 9), and the Fe-Ti oxide and epidote models are from Holland and Powell (1998). Chlorite activity model is from Holland *et al.* (1998). The other phases are pure end-members: brucite, magnetite, and H_2O. The small-scale heterogeneities in serpentinite do not allow performing XRF analyses of an "equilibrium rock volume". Therefore rock compositions (Figure 7b and Figure 7c) are estimated integrating modal proportions by polarised light microscope analysis with the phase compositions acquired by WDS analysis. Compositions obtained have also been validated with EDS analysis of an area of 3 mm^2 of the same thin sections.

After studying several samples, two (with clinopyroxene and with olivine, respectively, in the D2 assemblages - Figure 7b and Figure 7c) were chosen as representative, as in both S2 is dominant and no relics of previous textures are preserved.

Modal proportions used were:

- Atg 73, Ol 20, Mag 7 (Figure 7b)

- Atg 20, Cpx 55, Ilm 2, Chl 20, Mag 3 (Figure 7c).

O content was set to 0.76 and 1.5 respectively (mole proportions) from mineral analyses, where Fe^{3+} content was derived by charge balance, and also accounting for modal proportions of magnetite.

Because serpentine is > 40%, and is found in all HP assemblages together with Ol or Cpx, the modelling was performed with H_2O in excess (Guiraud *et al.* 2001; Rebay *et al.* 2010). Although Créton serpentinites are rich in Ti-humite minerals, the modelled samples are the poorest in Ti-phases in order to minimize Ti content in the bulk composition, as reliable a-x models for Ti-rich minerals are not available. In both the pseudosections, magnetite and H_2O are in excess. Bulk compositions have been calculated by the mode of the minerals, whose compositions are reported in Table 4.

In Figure 7b a pseudosection calculated for a sample with Ol - Atg - Mag bearing S2 foliation is presented. All fields are delimited by vertical curves. Divariant fields are narrow, spanning maximum over a range of 10°C, whereas trivariant and quadrivariant fields are wider, and all fields are stable within the whole range of considered pressures from 1 to 4 GPa. Chlorite is stable at T < 580 °C and orthopyroxene is stable at T > 592 °C. Even if this is a Cpx-free sample, olivine and diopside are predicted to be stable in every field. It is though important to note that in the Ol - Di - Atg field, constrained between 560 and 640 °C by the Chl-out and Opx-in curves, the predicted Cpx mode is negligible (<0.1%), and therefore this field represents the assemblage we actually observe in the rock.

The pseudosection of Figure 7c is calculated for the composition of a rock where clinopyroxene is found in D2 together with Atg - Chl - Mag. Fields are again mostly separated by vertical boundaries as already seen in the olivine-bearing rock, but a horizontal divariant field with Di - Atg - Chl - Mag, separates at lower temperatures (<650°C) a field where actinolite is stable at P < 1.6 -1.8 GPa from a field where Ta is stable with Di - Atg - Chl (and Mag) for P > 1.7 GPa. This latter field represents the assemblage observed in our sample, once it is realised that the predicted Ta mode in this field is < 2%. D3 assemblage stability conditions are constrained by the predicted coexistence of actinolite and antigorite at P < 1.7 GPa.

In this latter case, Cpx and Ol have never been observed in the same assemblage, and it is therefore impossible to further constrain PT conditions by using isopleths of these two phases as done in Rebay *et al.* 2012, in samples from nearby outcrops. Rebay *et al.* (2012) estimated for D2 2.5 ± 0.3 GPa and 600 ± 20°C, and for D3 1 ± 0.4 GPa and 550 ± 50°C, as indicated in Figure 7a and Figure 7b with dashed and dotted polygons.

On the other hand, the Opx-in curve in Figure 7b (Ol-rich assemblage), calculated for syn-D2 conditions in serpentinite, can be superposed to the PT fields of the pre-D2 and pre-D2-to-early-D2 stages (Figure 7a), to further constrain their conditions.

In fact, in serpentinite, pre-D2 and D2 assemblages are characterised by the same chemical system, and Opx never occurs neither in pre-D2 nor in D2 assemblage. The Opx-in curve, calculated for D2 assemblage in serpentinite, represents therefore a temperature constrain also for pre-D2 stage. Likely, Ti-Chn + Ti-Chu veins, which formed before D2 stage and occur in the same serpentinite outcrops of the samples used for estimating syn-D2 conditions, do not contain Opx. Then, Opx-in curve from Ol-rich assemblage (Figure 7b) is preferred to Opx-in curve from Cpx-rich assemblage (Figure 7c), since no Cpx occurs in Figure 7a.

The superposition of the Opx-in curve from the Ol-rich assemblage pseudosection (red curve in Figure 7a) let decrease T_{max} from 670 to 630 °C and P_{max} from 3.5 to 3.3 GPa. Therefore, new pre-D2 PT conditions can be proposed as P = 2.8-3.3 GPa and 600-630 °C. In the same way, pre-D2-to-early-D2 conditions can be delimited by Opx-in curve: T_{max} is reduced to 630 °C and P_{max} to 2.9 GPa. The P-T-d-t path of the Créton serpentinites sinthesyses in Figure 7d the P-T conditions inferred for the successive deformation stages.

7. Geodynamic modelling and tectonic history

7.1 Setup

We used the 2D finite element method to simulate an ocean-continent subduction (Regorda *et al.* 2017) in order to compare the tectono-metamorphic history of serpentinites of the ZSZ with the evolution of the oceanic lithosphere within a subduction zone, since in the literature a continental upper plate is proposed for the Alpine subduction system (Dal Piaz *et al.* 1972; Polino *et al.* 1990; Roda *et al.* 2012 and reference therein). The physics of the crust-mantle system is described by coupled equations for continuity, conservation of momentum, and conservation of energy (Marotta *et al.* 2006). The equations are solved by means of the 2D finite element code Submar (Marotta *et al.* 2006), which includes erosion and sedimentation processes (Roda *et al.* 2012), shear heating (Regorda *et al.* 2017), and oceanic crust dehydration and mantle serpentinisation mechanisms (Meda *et al.* 2010; Roda *et al.* 2010; Roda *et al.* 2012). According to Regorda *et al.* (2017), a viscous rheology is assumed for the sublithospheric mantle and a brittle/plastic rheology is assumed for the lithosphere. Materials are compositionally differentiated via the Lagrangian markers technique (Christensen 1992), by using 1 marker per 0.25 km^2 to define the atmosphere/water, the sediments, the upper and lower oceanic crust, the continental crust, and the mantle. During the evolution of the system, each marker is advected in time and in space using a first order Runge–Kutta scheme (Marotta and Spalla 2007; Roda *et al.* 2010; Roda *et al*. 2012; Regorda *et al*. 2017; Regorda *et al*. 2020). The material and rheological parameters used in the simulation are listed in Table 5.

An initial continental lithospheric thickness of 80 km, including 30 km of continental crust, is assumed (Figure 8) to represent the originally thinned passive margin that characterised the former margin of Adria (Dal Piaz 2001; Marotta *et al.* 2018; Roda *et al.* 2019). An oceanic lithospheric thickness of 80 km is chosen to represent an age of ca. 40 Myr for the Tethys Ocean (Handy *et al.* 2010; Roda *et al.* 2012), based on the cooling model of a semi-infinite half-space (Turcotte and Schubert 2002), and characterised by a slow spreading rate (2.5 cm/yr full spreading). The upper oceanic crust is generally strongly affected by hydrothermal alteration at mid-ocean ridges, thermal fracturing, and it is covered by oceanic sediments. Furthermore, intense serpentinisation affects the oceanic mantle that can be episodically exhumed at ocean floor (Carlson and Miller 1997; Juteau and Maury 1999; Christensen 2004; Malvoisin *et al.* 2012; Cannat *et al.* 2013). For this reason, the upper oceanic crust is assumed to be composed by a 5 km-thick layer of porous and fractured basalts and serpentinites. Compared to the upper oceanic crust, the lower oceanic crust is considered to be little affected by hydrothermal circulation and mainly formed by gabbros (Carlson and Miller 1997; Canales *et al*. 2000; Christensen 2004; Malvoisin *et al.* 2012; Cannat *et al*. 2013; Rüpke and Hasenclever 2017). Therefore, the lower oceanic crust is represented by a 5 km-thick layer with the rheology of a dry diabase.

To simulate plate convergence, a horizontal velocity of 3 cm/yr is imposed along the bottom of the oceanic crust (Roda *et al.* 2012; Roda *et al.* 2010) and the initial slab dip is 45° (Roda *et al.* 2010). The model runs for 65 Myr of oceanic subduction, i.e. from 100 to 35 Ma (Hunziker *et al.* 1992; Handy and Oberänsli 2004; Handy *et al.* 2010; Roda *et al.* 2012). Additional details about the model setup are summarised in the caption of Figure 8.

7.2 Model results

The subduction of the oceanic lithosphere induces the tectonic erosion of part of the continental crust from the overriding plate due to the strong coupling along the plate boundary. The burial flow carries the oceanic and continental crust, trench sediments and mantle markers toward deep levels of the subduction zone. The hydrated upper oceanic crust progressively releases fluids within the mantle wedge during the burial, and serpentinisation of the overriding mantle occurs. The size of the serpentinised mantle wedge increases with time due to the continuous dehydration of the upper oceanic crust and the progressive cooling of the subduction system. The strong contrast between serpentinites and dry mantle results in an intense counterclockwise convection flow developed in the upper part of the mantle wedge. As a consequence, part of the subducted material is exhumed to shallower structural levels within the mantle wedge and the rest remains in the deeper portion of the mantle wedge or is inhumed in the sublithospheric mantle. The upper oceanic crust is commonly involved in the exhumation process, sometimes coupled with recycled trench sediments. During the exhumation within the mantle wedge, the oceanic crust can also be coupled with dry continental mantle and continental crust coming from the upper plate.

The result of such a tectonic mingling is a subduction-related mélange comprising a mixture of exhumed upper oceanic and continental crustal slices, buried and exhumed trench sediments, and continental lithospheric mantle enclosed within the serpentinised matrix derived from the hydrated mantle wedge. The subducted materials record different PT peak conditions, different P-T-t evolutions and different exhumation trajectories, and the size of a single tectono-metamorphic unit ranges from 2-3 km^2 to several tens of km^2, which is consistent with the results already discussed by Roda *et al.* (2012).

7.3 Natural data vs model predictions

The inferred P-T-d-t path of Créton serpentinites (Figure 7d) is compared with the tectonic setting and thermal state predicted by the numerical model of an ocean-continent subduction zone. Since ZSZ serpentinites have been interpreted as affected by ocean floor metasomatism, therefore representing the upper part of the oceanic lithosphere, we focus on the geological setting recorded by the markers that belong to the upper oceanic crust at different timing of the tectono-metamorphic history. The first structural and metamorphic re-equilibration predates D2, and the serpentinites recorded the peak conditions at pressure of 2.8-3.3 GPa and temperature of 600-630°C (Figures 7 and 9). There is no radiometric age associated with this stage, but pre-D2 structures are clearly older than D2 stage, which has been dated 60-70 Ma by Rebay *et al.* (2018). The oldest age proposed for the prograde path of ZSZ is 80 Ma (Skora *et al.* 2009). Therefore, we extrapolate two main events of the numerical simulation to be compared with the pre-D2 stage at steps of 80 and 72 Ma (Figure 9). For the oldest event (80 Ma), the pre-D2 PT conditions occur in the portion of the upper oceanic crust within the serpentinised mantle wedge still close to the slab (Figure 9a). The lithological mixing is poor and only few markers of trench sediments record the same PT conditions (Figure 9a). Pre-D2 conditions can be also potentially reached by a portion of the lithospheric oceanic mantle below the Benioff plane (Figure 9a). However, this portion has been excluded for the comparison because the ocean floor metasomatism, widely testified in the ZSZ oceanic lithosphere of upper Valtournanche, does not occur below the Benioff plane. In the simulated system, pre-D2 conditions occur at a distance of 100-130 km from the trench and at ca. 80-110 km depth (Figure 9a and Figure 9b). At 72 Ma, the size of the serpentinised mantle wedge increases, and the pre-D2 PT conditions extend to an innermost portion of the mantle wedge (Figure 9c). The lithological mixing is still poor and characterised by upper oceanic crust and few sediment markers. Again, the portion of the lithospheric oceanic mantle below the Benioff plane recording pre-D2 conditions can be excluded from the comparison, for the occurrence of ocean floor metasomatism. The fitting of pre-D2 PT conditions in the subduction system is accomplished at a distance of 110-145 km from the trench and at ca. 80-110 km depth (Figure 9c and Figure 9d).

The D2 stage represents the first exhumation stage recorded by Créton serpentinites and occurs at P and T conditions of 1.8-2.8 GPa and 580-620°C. The D2 radiometric age varies from 70 to 60 Ma and, therefore, we compare D2 PT conditions with three different time steps of the simulation: 70, 65, and 60 Ma (Figure 10). In the oldest step (70 Ma), D2 conditions are recorded by markers of upper oceanic crust within the mantle wedge, coupled with rare markers of trench sediments and some markers of continental crust (Figure 10a). In the successive steps, the amount of trench sediments recording D2 conditions sensibly increases (Figure 10c and Figure 10e). With the size increase of the serpentinised mantle wedge with time, the area characterised by PT conditions fitting with those of D2 moves away from the slab (Figure 10a, Figure 10c, and Figure 10e), and the maximum distance from the trench varies from 125 km at 70 Ma to 155 km at 60 Ma (Figure 10b, Figure 10d, and Figure 10f). Starting from the oldest age, depth varies between 85 and 55 km.

The D3 stage occurred under epidote-amphibolite facies conditions (Rebay *et al.* 2012) and intermediate PT ratio, compatible with a Barrovian metamorphism. Therefore, D3 PT conditions likely occurred at the end of the oceanic subduction, at the beginning of the continental collision (Regorda *et al.* 2017).

8. Discussions

Results of this integrated structural, petrological, and modelling approach on Créton serpentinites show that rocks that are generally considered cryptic, preserve a wealth of information to be disclosed, that in this case-study results into the reconstruction of a complex polydeformed and polymetamorphosed lithostratigraphy of a portion of oceanic crust. Serpentinites, with magnetite layers and Ti-chondrodite + Ti-clinohumite veins, embed pyroxenites, diopsidites, and Ol-rich layers. Serpentinites preserve various types of pre-D2 relics within the S2 foliation, such as D1 rootles folds, S1 foliation, porphyroclasts, and polygonal mineral aggregates. D2 stage produced isoclinal folds and the dominant fabric, which is the S2 mylonitic foliation; D3 crenulated S2 and is associated with discrete shear zones.

By reconstructing the successive mineral assemblages, and the definition of the PT conditions registered by serpentinites, the correlation of the fabrics of Créton outcrops with those described by Rebay *et al.* (2012) and Zanoni *et al.* (2012; 2016) was possible. The pre-D2 (Ti-Chn + Atg + Spl ± Chl + Ol/Cpx) and pre-D2-to-early-D2 (Ti-Chn + Ti-Chu + Atg + Ilm + Mag + Ol/Cpx) assemblages in Ti-Chondrodite + Ti-Clinohumite veins indicate pressure and temperature ranges of 2.8-3.3 GPa and 600-630 °C, and 2.1-3.0 GPa and 570-670 °C, respectively (Figure 7a).

The integration of the petrological modelling of syn-D2 PT conditions for Cpx + Atg + Mag + Chl- and Ol + Atg + Mag-bearing S2 foliation in serpentinites suggests pressures greater than 1.8 GPa and temperatures between 540 and 640 °C. Since Ol and Cpx never occur together along S2 foliation, these results represent the best ones obtainable for these assemblages and, at the same time, they confirm those proposed for the S2 assemblage developed in adjacent serpentinites and rodingites (Rebay *et al.* 2012; Zanoni *et al.* 2016) at 2.2-2.8 GPa and 580-620 °C, which has been dated at 60-70 Ma (Rebay *et al.* 2018). Furthermore, although referred to different compositional systems, the calculated curve of Opx-in for syn-D2 assemblages in serpentinites have been used to better constrain pre-D2 and pre-D2-to-early-D2 metamorphic conditions of Ti-Chn + Ti-Chu veins, since these veins formed before the D2 stage. The new proposed conditions are characterised by pressure and temperature ranges of 2.8-3.3 GPa and 600-630 °C for pre-D2 stage, and 2.1-2.9 GPa and 570-630 °C for pre-D2-to-early-D2 stage.

The comparison between PT conditions for pre-D2 and D2 stages and the prediction of a numerical model of an ocean-continent subduction allowed inferring a vertical "palaeogeography" for the serpentinites during their evolution between 80 and 60 Ma in the subduction system. The model suggests that, between 80 and 72 Ma, markers of upper oceanic crust that represent the Créton serpentinites attained pre-D2 PT conditions at a distance from the trench ranging from 100 km to 145 km, at depths of 80-110 km. D2 PT conditions were attained by markers located at a distance from the trench from 125 km at 70 Ma to 155 km at 60 Ma, for depths between 85 and 55 km.

At pre-D2 PT conditions, the lithological mixing between oceanic markers and trench sediments is poor, and the continental markers are rare or absent. On the other hand, at D2 PT conditions, the lithological mixing between oceanic markers and trench sediments sensibly increases and some continental markers attained the same PT conditions. Therefore, the coupling between rodingite-bearing serpentinites of ZSZ, metasediments, and continental slices (e.g. Weber and Bucher 2015) is more likely attained during D2, still under eclogite facies conditions (Weber *et al.* 2015). D2 developed during the earlier stages of exhumation of Créton serpentinites under P/T ratios consistent with ongoing oceanic subduction, and thus long before the continental collision onset. This interpretation is also consistent with the strong parallelisation of Valtournanche lithostratigraphic surfaces with S2 foliation.

Finally, considering different radiometric ages proposed for UHP conditions in ZSZ, we also compared the PT peak estimates for the Cignana Lake Unit with the model predictions at 40 Ma (Table 1; Figure 11). At 40 Ma several markers of oceanic crust and trench sediments achieved the PT conditions proposed for the Cignana Lake Unit (i.e. 2.6-3.0 GPa and 590-630 °C). This fitting supports the idea of continuous subduction and exhumation of crustal material over the simulated 65 Myr and explain the occurrence of different peak ages and different UHP conditions in slices accreted in ZSZ. The proposed geodynamics is not peculiar for the Alpine chain only. A similar syn-subductive evolution, characterised by a deep and cold subduction, is also proposed for the Palaeozoic serpentinites in La Cabaña area of the Chilean Coastal Cordillera (González-Jiménez *et al.* 2017).

9. Conclusions

The integration of different approaches in this study adds a new UHP puzzle tile to ZSZ tectonic evolution. The Créton serpentinite reached UHP conditions (2.8-3.3 GPa and 600-630 °C) before the development of the dominant S2 foliation, which has been dated at 60 - 70 Ma and represents an exhumation-related tectono-metamorphic stage. At the regional scale, this new UHP finding reinforces the idea of a heterogeneous nature of ZSZ, that can be therefore interpreted as constituted by different tectono-metamorphic units, which were amalgamated and partly obliterated during the development of the dominant regional S2 foliation under UHP-HP conditions. The vertical restoration of Créton serpentinite during subduction is here reconstructed by comparing the P-T-t-d path with 2D model predictions and suggests that the pre-D2 re-equilibration took place at around 100 km depth, close to the slab, before 70 Ma. Afterwards, these rocks were exhumed and migrated toward the top of the serpentinised wedge where syn-D2 assemblages developed between 60 and 80 km depth: here Ti-humite-bearing serpentinites were tectonically mixed with trench sediments and minor slices of continental crust.

The good agreement of the inferred tectono-metamorphic evolution compared with the predictions of the quantitative geodynamic modelling of an ocean-continent subduction system, together with the heterogeneous and diachronic metamorphic evolutions inferred in different portions of ZSZ, suggests that ophiolites from the axial zone of the Alpine belt can be considered as a tectonic mélange of different oceanic lithospheric slices that recorded different thermal and structural evolutions during their burial and exhumation trajectories in the mantle wedge of the subduction system.

Acknowledgments

The authors acknowledge insightful reviews by Kurt Bucher and an anonymous reviewer that greatly improved the text. C. Malinverno prepared thin sections and A. Risplendente assisted the work at the microprobe. Results here presented have been developed in the frame of the MIUR Project "Dipartimenti di Eccellenza 2017 - Le geoscienze per la società: risorse e loro evoluzione (Work-package 3, Tasks 3.3-3.4)". P.L. thanks Paolo Papone and Ugo Zuretti for their kind hospitality during fieldwork.

Funding

This work was supported by the University of Milano under Grant [PSR2018_DZANONI] and MIUR under Grant [FFABR2018DZANONI]. Studio Ciocca supported P.L.'s PhD scholarship.

References

Afonso, J.C., and Ranalli, G., 2004, Crustal and mantle strengths in continental lithosphere: is the jelly sandwich model obsolete?: Tectonophysics, v. 394, p. 221-232. doi: 10.1016/j.tecto.2004.08.006

Amato, J.M., Johnson, C.M., Baumgartner, L.P., and Beard, B.L., 1999, Rapid exhumation of the Zermatt-Saas ophiolite deduced from high precision Sm-Nd and Rb-Sr geochronology: Earth and Planetary Science Letters, v. 171, p. 425-38.

Angiboust, S., and Agard, P., 2010, Initial water budget: The key to detaching large volumes of eclogitized oceanic crust along the subduction channel?: Lithos, v. 120, p. 453-474. doi: 10.1016/j.lithos.2010.09.007

Angiboust, S., Agard, P., Jolivet, L., and Beyssac, O., 2009, The Zermatt-Saas ophiolite: The largest (60-km wide) and deepest (c. 70-80km) continuous slice of oceanic lithosphere detached from a subduction zone?: Terra Nova, v. 21, p. 171-180. doi: 10.1111/j.1365-3121.2009.00870.x

Balestro, G., Festa A., and Dilek, Y., 2019, Structural architecture of the western alpine ophiolites, and the Jurassic seafloor spreading tectonics of the Alpine Tethys: Journal of the Geological Society, v. 176, p. 913-930. doi: 10.1144/jgs2018-099

Barnicoat, A.C., 1988, Zoned high-pressure assemblages in pillow lavas of the Zermatt-Saas ophiolite zone, Switzerland: Lithos, v. 21, p. 227-36.

Barnicoat, A.C., and Fry, N., 1986, High-pressure metamorphism of the Zermatt-Sass ophiolite, Switzerland: Journal of the Geological Society, v. 143, p. 607-618.

Bearth, P., 1967, Die ophiolite der Zone von Zermatt-Sass Fee: Beitrag Geologische Karte Schweitz, v. 132, p. 1-130.

Beltrando, M., Rubatto, D., and Manatschal, G., 2010, From passive margins to orogens: The link between ocean-continent transition zones and (ultra)high-pressure metamorphism: Geology, v. 38, p. 559-562. doi: 10.1130/G30768.1

Best, M.G., and Christiansen, E.H., 2001, Igneous Petrology: Blackwell Science, Oxford, 458 p.

Bigi, G., Cosentino, D., Parotto, M., Sartori, R., and Sandone, P., 1990, Structural Model of Italy and gravity map. Scale 1: 500.000, Sheets 1-9 C.N.R., Progetto finalizzato Geodinamica: Quaderni de «La Ricerca Scientifica», no 114.

Bousquet, R., Engi, M., Gosso, G., Oberhänsli, R., Berger, A., Spalla, M.I., Zucali, M., and Goffè, B., 2004, Explanatory notes to the map: Metamorphic structure of the Alps Transition from the Western to the Central Alps: Mitteilungen der Österreichischen Mineralogischen Gesellschaft, v. 149, p. 145-156.

Bowtell, S.A., Cliff, R.A., and Barnicoat, A.C., 1994, Sm-Nd isotopic evidence on the age of eclogitisation in the Zermatt-Saas ophiolite: Journal of Metamorphic Geology, v. 12, p. 187-96.

Bucher, K., Fazis, Y., de Capitani, C., and Grapes, R., 2005, Blueschists, eclogites, and decompression assemblages of the Zermatt-Saas ophiolite: High-pressure metamorphism of subducted Tethys lithosphere: American Mineralogist, v. 90, p. 821-835. https://doi.org/10.2138/am.2005.1718

621 Bucher, K. and Frey, M., 1994. Petrogenesis of Metamorphic Rocks. Heidelberg, Berlin: Springer,
622 318 pp.

623 Bucher, K., and Grapes, R., 2009, The eclogite-facies Allalin gabbro of the Zermatt-Saas ophiolite,
624 Western alps: A record of subduction zone hydration: Journal of Petrology, v. 50, p. 1405-
625 1442. doi: 10.1093/petrology/egp035

626 Canales, J.P., Detrick, R.S., Lin, J., Collins, J.A., and Toomey, D.R., 2000, Crustal and upper
627 mantle seismic structure beneath the rift mountains and across a non-transform offset at the
628 Mid-Atlantic Ridge (35°N): Journal of Geophysical Research - Solid Earth, v. 105, p.
629 2699-2719. doi: 10.1029/1999JB900379

630 Cannat, M., Fontaine, F., and Escartín, J., 2013, Serpentinisation and Associated Hydrogen and
631 Methane Fluxes at Slow Spreading Ridges. Diversity of Hydrothermal Systems on Slow
632 Spreading Ocean Ridges. American Geophysical Union, Abstract, p. 241-264. doi:
633 10.1029/2008GM000760

634 Carlson, R.L., and Miller, D.J., 1997, A new assessment of the abundance of serpentinite in the
635 oceanic crust: Geophysical Research Letters, v. 24, p. 457-460. doi: 10.1029/97GL00144

636 Chinner, G.A. and Dixon, J.E., 1973, Some high pressure parageneses of the Allalin gabbro, Valais,
637 Switzerland: Journal of Petrology, v. 14, p. 185-202.

638 Chopin, C., 1984, Coesite and pure pyrope in high-grade blueschists of the Western Alps: a first
639 record and some consequences: Contributions to Mineralogy and Petrology, v. 86, p. 107-
640 118

641 Chopin, C., Klaska, R., Medenbach, O., and Dron, D., 1986, Ellenbergerite, a new high-pressure
642 Mg-Al-(Ti,Zr)-silicate with a novel structure based on face-sharing octahedral:
643 Contributions to Mineralogy and Petrology, v. 92, p. 316-321.

644 Chopra, P.N., and Paterson, M.S., 1981, The experimental deformation of dunite: Tectonophysics,
645 v. 78, p. 453-473. doi: 10.1016/0040-1951(81)90024-X

646 Christensen, U.R., 1992, An Eulerian Technique for thermo-mechanical model of lithospheric
647 extension: Journal of Geophysical Research, v. 97, p. 2015-2036. doi: 10.1029/91JB02642

Christensen, N.I., 2004, Serpentinites, Peridotites, and Seismology: International Geology Review, v. 46, p. 795-816. doi: 10.2747/0020-6814.46.9.795

Cloos, M., 1993, Lithospheric buoyancy and collisional orogenesis: subduction of oceanic plateaus, continental margins, island arcs, spreading ridges, and seamounts: Geological Society of America Bulletin, v. 105, p. 715-737.

Dal Piaz, G.V., 1988, Revised setting of the Piemonte zone between Valtournanche and Gressoney valleys: Ofioliti, v. 13, p. 157-162.

_____ 1992, Guida geologica: Le Alpi dal Monte Bianco al Lago Maggiore, v. 3, Seven Hills Book.

_____ 1999, The Austroalpine-Piedmont nappe stack and the puzzle of Alpine Tethys: Memorie di Scienze Geologiche, v. 51, p. 155-176.

_____ 2001, History of tectonic interpretations of the Alps: Journal of Geodynamics, v. 32, p. 99-114. doi: /10.1016/S0264-3707(01)00019-9

_____ 2010, The Italian Alps: A journey across two centuries of Alpine geology: Journal of the Virtual Explorer, v. 36, paper 8. doi: 10.3809/jvirtex.2010.00234

Dal Piaz, G.V., and Ernst, W.G., 1978, Areal geology and petrology of eclogites and associated metabasites of the Piemonte ophiolite nappe, Breuil-St. Jacques area, Italian Western Alps: Tectonophysics, v. 51, p. 99-126.

Dal Piaz, G.V., Hunziker, J.C., and Martinotti, G., 1972, La zona Sesia-Lanzo e l'evoluzione tettonico-metamorfica delle Alpi nord-occidentali interne: Memorie della Società Geologica Italiana, v. 11, p. 433-460.

Dal Piaz, G.V., Venturelli, G., Spadea, P., and Di Battistini, G., 1981, Geochemical features of metabasalts and metagabbros from the Piemonte ophiolite nappe, Italian Western Alps: Neues Jahrbuch für Mineralogie – Abhandlungen, v. 142, p. 248-269.

Dale, C.W., Burton, K.W., Pearson, D.G., Gannoun, A., Alard, O., Argles, T.W., and Parkinson, I.J., 2009, Highly siderophile element behaviour accompanying subduction of oceanic crust: Whole rock and mineral-scale insights from a high-pressure terrain: Geochimica et Cosmochimica Acta, v. 73, p. 1394-1416. doi: 10.1016/j.gca.2008.11.036

Deer, W.A., Howie, R.A., and Zussman, J., 1992, An Introduction to the Rock Forming Minerals: Longman, 712 p.

De Giusti, F., Dal Piaz, G.V., Schiavo, A., Massironi, M., Monopoli, B., Bistacchi, A., and Schiavo, A., 2003, Carta geotettonica della Valle d'Aosta: Memorie di Scienze Geologiche, v. 55, p. 129-149.

De Hoog, J.C.M., Gall, L., and Cornell, D.H., 2010, Trace-element geochemistry of mantle olivine and application to mantle petrogenesis and geothermobarometry: Chemical Geology, v. 270, p. 196-215. doi : 10.1016/j.chemgeo.2009.11.017

Diener, J.F.A., Powell, R., White, R.W., and Holland, T.J.B., 2007, A new thermodynamic model for clino- and orthoamphiboles in the system Na_2O-CaO-FeO-MgO-Al_2O_3-SiO_2-H_2O-O: Journal of Metamorphic Geology, v. 25, p. 631-656. doi: 10.1111/j.1525-1314.2007.00720.x

Droop, G.T.R., 1987, A general equation for estimating Fe^{3+} concentrations in ferromagnesian silicates and oxides from microprobe analyses, using stoichiometric criteria: Mineralogical Magazine, v. 51, p. 431-435doi: 10.1180/minmag.1987.051.361.10

Dubois, J., and Diament, M., 1997, Géophysique: Masson, Paris.

Ernst, W.G., and Dal Piaz, G.V., 1978, Mineral parageneses of eclogitic rocks and related mafic schists of the Piemonte ophiolite nappe, Breuil-St. Jacque: American Mineralogist, v. 63, p. 621-640.

Ernst, W.G., and Liou, J.G., 1999, Overview of UHP metamorphism and tectonics in well-studied collisional orogens: International Geology Review, v. 41, p. 477-493.

Fassmer, K., Obermüller, G., Nagel, T.J., Kirst, F., Froitzheim, N., Sandmann, S., Miladinova, I., Fonseca, R.O.C., and Münker, C., 2016, High-pressure metamorphic age and significance of eclogite-facies continental fragments associated with oceanic lithosphere in the Western Alps (Etirol-Levaz Slice, Valtournenche, Italy): Lithos, v. 252-253, p. 145-159. doi: 10.1016/j.lithos.2016.02.019

Ferracutti, G.R., Gargiulo, M.F., Ganuza, M.L., Bjerg, E.A., and Castro, S.M., 2015, Determination of the spinel group end-members based on electron microprobe analyses: Mineralogy and Petrology, v. 109, p. 153-160. doi: 10.1007/s00710-014-0363-1

Ferrando, S., Frezzotti, M.L., Orione, P., Conte, R.C., and Compagnoni, R., 2010, Late-Alpine rodingitisation in the Bellecombe meta-ophiolites (Aosta Valley, Italian Western Alps): evidence from mineral assemblages and serpentinisation-derived H_2-bearing brine: International Geology Review, v. 52, p. 1220-1243. doi: 10.1080/00206810903557761

Ferraris, G., Ivaldi, G., and Chopin, C., 1995, Magnesiodumortierite, a new mineral from very-high-pressure rocks (Western Alps). Part I: Crystal structure: European Journal of Mineralogy, v. 7, p. 167-174. doi: 10.1127/ejm/7/1/0167

Forster, M., Lister, G.S., Compagnoni, R., Giles, R., Hills, D., 2004, Mapping of oceanic crust with "HP" to "UHP" metamorphism: The Lago di Cignana Unit, (Western Alps), *in* Pasquarè, G. Venturini, C. & Groppelli, G. eds, Mapping Geology in Italy. APAT - Dip. Difesa del Suolo, Servizio Geologico d'Italia, Roma 2004 (2006), Map 33, printed by S.EL.CA. Firenze, p. 279-286.

Frezzotti, M.L., Selverstone, J., Sharp, Z.D., and Compagnoni, R., 2011, Carbonate dissolution during subduction revealed by diamond-bearing rocks from the Alps: Nature Geoscience, v. 4, p. 703-706. doi: 10.1038/ngeo1246

Gerya, T.V., and Stöckhert, B., 2005, Two-dimensional numerical modeling of tectonic and metamorphic histories at active continental margins: International Journal of Earth Science, v. 95, p. 250-274. doi: 10.1007/s00531-005-0035-9

Gerya, T.V., and Yuen, D.A., 2003, Characteristics-based marker-in-cell method with conservative finite-differences schemes for modeling geological flows with strongly variable transport properties: Physics of the Earth and Planetary Interiors, v. 140, p. 293-318. doi: 10.1016/j.pepi.2003.09.006

Gilio, M., Scambelluri, M., Agostini, S., Godard, M., Peters, D., and Pettke, T., 2019, Petrology and Geochemistry of Serpentinites Associated with the Ultra-High Pressure Lago di Cignana Unit (ItalianWestern Alps): Journal of Petrology, v. 60, 1229–1262. doi: 10.1093/petrology/egz030

González-Jiménez, J.M., Plissart, G., Garrido, L.N., Padrón-Navarta, J.A., Aiglsperger, T., Romero, R., Marchesi, C., Moreno-Abril, A.J., Reich, M., Barra, F., and Morata, D., 2017, Titanian clinohumite and chondrodite in antigorite serpentinites from Central Chile: evidence for deep and cold subduction: European Journal of Mineralogy, v. 29, p. 959-970.

Gouzu, C., Itaya, T., Hyodo, H., and Matsuda, T., 2006, Excess ^{40}Ar-free phengite in ultrahigh-pressure metamorphic rocks from the Lago di Cignana area, Western Alps: Lithos, v. 92, p. 418-30.

Groppo, C., Beltrando, M., and Compagnoni, R., 2009, The P-T path of the ultra-high pressure Lago Di Cignana and adjoining high-pressure meta-ophiolitic units: Insights into the evolution of the subducting Tethyan slab: Journal of Metamorphic Geology, v. 27, p. 207-231doi: 10.1111/j.1525-1314.2009.00814.x

Groppo, C., and Compagnoni, R., 2007, Metamorphic veins from the serpentinites of the Piemonte Zone, western Alps, Italy: A review: Periodico di Mineralogia, v. 76, p. 127-153. doi: /10.2451/2007PM0021

Guiraud, M., Powell, R., and Rebay, G., 2001, H_2O in metamorphism and unexpected behaviour in the preservation of metamorphic mineral assemblages: Journal of Metamorphic Geology, v. 19, p. 445-454. doi: 10.1046/j.0263-4929.2001.00320.x

Haenel, R., Rybach, L., and Stegena, L., 1988, Handbook of Terrestrial Heat-Flow Density Determination: Kluwer Academic Publishers, p. 125-142. doi: 10.1007/978-94-009-2847-3

Handy, M.R., and Oberhänsli, R., 2004, Explanatory notes to the map: metamorphic structure of the Alps age map of the metamorphic structure of the Alps – tectonic interpretation and outstanding problems: Mitteilungen der Österreichischen Mineralogischen Gesellschaft, v. 149, p. 201-225.

Handy, M.R., Schmid, S.M., Bousquet, R., Kissling, and E., Bernoulli, D., 2010, Reconciling plate-tectonic reconstructions of Alpine Tethys with the geological-geophysical record of spreading and subduction in the Alps: Earth-Science Reviews, v. 102, p. 121-158. doi: 10.1016/j.earscirev.2010.06.002

757 Holland, T.J.B., Baker, J., and Powell, R., 1998, Mixing properties and activity-composition
758 relationships of chlorites in the system MgO-FeO-Al_2O_3-SiO_2-H_2O: European Journal of
759 Mineralogy, v. 10, p. 395-406. doi: 10.1127/ejm/10/3/0395

760 Holland, T.J.B., and Powell, R., 1998, An internally consistent thermodynamic data set for phases
761 of petrological interest: Journal of Metamorphic Geology, v. 16, p. 309-343. doi:
762 10.1111/j.1525-1314.1998.00140.x

763 Hunziker, J.C., Desmons, J., and Hurford, A.J., 1992, Thirty-two years of geochronological work in
764 the Central and Western Alps: a review on seven maps: Mémoires de Géologie (Lausanne),
765 v. 13, p. 1-59.

766 Juteau, T., and Maury, R., 1999, The Oceanic Crust, From Accretion to Mantle Recycling:
767 Springer-Verlag, New York, 390 p.

768 Kienast J.R., Lombardo, B., Biino, G., and Pinardon, J.L., 1991, Petrology of very-high-pressure
769 eclogitic rocks from the Brossasco-Isasca complex, Dora-Maira massif, Italian western
770 Alps: Journal of Metamorphic Geology, v. 9, p. 19-34.

771 Kirby, S.H., 1983, Rheology of the Lithosphere: Review of Geophysics, v. 21, p. 1459-1487. doi:
772 10.1029/RG021i006p01458

773 Li, X.P., Rahn, M., and Bucher, K., 2004a, Serpentinites of the Zermatt-Saas ophiolite complex and
774 their texture evolution: Journal of Metamorphic Geology, v. 22, p. 159-177. doi:
775 10.1111/j.1525-1314.2004.00503.x

776 ____ 2004b, Metamorphic processes in rodingites of the Zermatt-Saas ophiolites: International
777 Geology Review, v. 46, p. 28-51. doi: 10.2747/0020-6814.46.1.28

778 Locock, A.J., 2014, An Excel spreadsheet to classify chemical analyses of amphiboles following the
779 IMA 2012 recommendations: Computers and Geosciences, v. 62, p. 1-11. doi:
780 10.1016/j.cageo.2013.09.011

781 Luoni, P., Rebay, G., Spalla, M.I., and Zanoni, D., 2018, UHP Ti-chondrodite in the Zermatt-Saas
782 serpentinite: Constraints on a new tectonic scenario: American Mineralogist, v. 103, p.
783 1002-1005.

Luoni, P., Zanoni, D., Rebay, G., and Spalla, M.I., 2019, Deformation history of Ultra High-Pressure ophiolitic serpentinites in the Zermatt-Saas Zone, Créton, Upper Valtournanche (Aosta Valley, Western Alps): Ofioliti, v. 44, p. 111-123. doi: 10.4454/ofioliti.v44i2.468

Mahlen, N.J., Johnson, C.M., Baumgartner, L.P., Lapen, T.J., Skora, S., and Beard, B.L., 2006, The protracted subduction history and HP/UHP metamorphism of the Zermatt-Saas ophiolite, western Alps, as constrained by Lu-Hf geochronology: EOS Transactions AGU Fall Meeting, p. V41E-05.

Malvoisin, B., Brunet, F., Carlut, J., Rouméjon, S., and Cannat, M., 2012, Serpentinization of oceanic peridotites: 2. Kinetics and processes of San Carlos olivine hydrothermal alteration: Journal of Geophysical Research: Solid Earth, v. 117, p. 1-13. doi: 10.1029/2011JB008842.

Marotta, A.M., Roda, M., Conte, K., and Spalla, M.I., 2018, Thermo-mechanical numerical model of the transition from continental rifting to oceanic spreading: the case study of the Alpine Tethys: Geological Magazine, v. 155, p. 1-30. doi: 10.1017/S0016756816000856

Marotta, A.M., and Spalla, M.I., 2007, Permian-Triassic high thermal regime in the Alps: Result of late Variscan collapse or continental rifting? Validation by numerical modeling: Tectonics, v. 26, p. 1–30. doi: 10.1029/2006TC002047.

Marotta, A.M., Spelta, E., and Rizzetto, C., 2006, Gravity signature of crustal subduction inferred from numerical modelling: International Journal of Geophysics, v. 166, p. 923-938. doi: 10.1111/j.1365-246X.2006.03058.x

Martin, S., Tartarotti, P., and Dal Piaz, G.V., 1994, Alpine ophiolites: a review: Bollettino di Geofisica Teorica ed Applicata, v. 36, p. 175-219.

Meda, M., Marotta, A.M., and Spalla, M.I., 2010, The role of mantle hydration in continental crust recycling in the wedge region: Geological Society, London, Special Publications, v. 332, p. 149-172. doi: 10.1144/SP332.10

Meyer, J., 1983, Mineralogie und Petrologie des Allalingabbros [Ph.D. thesis]: Basel, Universität Basel.

Morimoto, N., 1988, Nomenclature of pyroxenes: Mineralogical Magazine, v. 52, p. 535-550.

Oberhänsli, R., 1980, PT bestimmungen anhand von mineral analysen in eklogiten und glaukophaniten der ophiolite von Zermatt: Schweizerische Mineralogische und Petrographische Mitteilungen, v. 60, p. 215-35.

Padrón-Navarta, J.A., López Sánchez-Vizcaíno, V., Hermann, J., Connolly, J.A.D., Garrido, C.J., Gómez-Pugnaire, M.T., and Marchesi, C., 2013, Tschermak's substitution in antigorite and consequences for phase relations and water liberation in high-grade serpentinites: Lithos, v. 178, p. 186-196. doi: 10.1016/j.lithos.2013.02.001.

Passchier, C.W., Myers, J.S., and Kroener, A., 1990, Field Geology of High-Grade Gneiss Terrains: Springer, Berlin, 150 pp.

Passchier, C.W., and Trouw, R.A.J., 2005, Microtectonics: Springer, Berlin, 366 pp.

Passeri, L., Ciarapica, G., and Dal Piaz, G.V., 2018, The problematic origin of the Pancherot-Cime Bianche-Bettaforca unit (PCB) in the Piemonte zone (Western Alps): Italian Journal of Geosciences, v. 137, p. 478-489. doi: 10.3301/IJG.2018.21

Polino, R., Dal Piaz, G.V., and Gosso, G., 1990, An accretionary wedge model for the pre-collisional Cretaceous orogeny in the Alps: Societé Géologique de France Memoires, v. 156, p. 309-321.

Powell, R., Holland, T.J.B., and Worley, B., 1998, Calculating phase diagrams involving solid solutions via non-linear equations, with examples using THERMOCALC: Journal of Metamorphic Geology, v. 16, p. 577-588.

Rahn, M., and Bucher, K., 1998, Titanian clinohumite formation in the Zermatt-Saas ophiolites, Central Alps: Mineralogy and Petrology, v. 64, p. 1-13. doi: 10.1007/BF01226561

Ranalli, G., and Murphy, D.C., 1987, Rheological stratification of the lithosphere: Tectonophysics, v. 132, p. 281-295. doi: 10.1016/0040-1951(87)90348-9

Rebay, G., Powell, R., and Diener, J.F.A., 2010, Calculated phase equilibria for a MORB composition in a P-T range, 450-650 °C and 18-28 kbar: the stability of eclogite: Journal of Metamorphic Geology, v. 28, p. 635-645. doi: 10.1111/j.1525-1314.2010.00882.x

Rebay, G., Spalla, M.I., and Zanoni, D., 2012, Interaction of deformation and metamorphism during subduction and exhumation of hydrated oceanic mantle: Insights from the Western Alps: Journal of Metamorphic Geology, v. 30, p. 687-702. doi: 10.1111/j.1525-1314.2012.00990.x

Rebay, G., Zanoni, D., Langone, A., Luoni, P., Tiepolo, M., and Spalla, M.I., 2018, Dating of ultramafic rocks from the Western Alps ophiolites discloses Late Cretaceous subduction ages in the Zermatt-Saas Zone: Geological Magazine, v. 155, p. 298-315. doi: 10.1017/S0016756817000334

Reddy, S.M., Wheeler, J., and Cliff, R.A., 1999, The geometry and timing of orogenic extension: an example from the Western Italian Alps: Journal of Metamorphic Geology, v. 17, p. 573-589.

Regorda, A., Lardeaux, J.-M., Roda, M., Marotta, A.M., and Spalla, M.I., 2020, How many subductions in the Variscan orogeny? Insights from numerical models: Geoscience Frontiers. doi: 10.1016/j.gsf.2019.10.005.

Regorda, A., Roda, M., Marotta, A.M., and Spalla, M.I., 2017, 2-D numerical study of hydrated wedge dynamics from subduction to post-collisional phases: Geophysical Journal International, v. 211, p. 974-1000. doi: 10.1093/gji/ggx336

Reinecke, T., 1991, Very high pressure metamorphism and uplift of coesite-bearing metasediments from the Zermatt-Saas Zone, Western Alps: European Journal of Mineralogy, v. 3, p. 7-17.

_____ 1995, Ultrahigh and high-pressure metamorphic rocks of the Zermatt-Saas zone, Western Alps records of burial and exhumation paths: Bochumer Geologische und Geotechnische Arbeiten, v. 44, p. 152-7.

_____ 1998, Prograde high- to ultrahigh-pressure metamorphism and exhumation of oceanic sediments at Lago di Cignana, Zermatt-Saas Zone, western Alps: Lithos, v. 42, p. 147-189. doi: 10.1016/S0024-4937(97)00041-8

Reinecke, T., van der Klauw, S.N.G.C., Stöckhert, B., 1994, UHP metamorphic oceanic crust of the Zermatt-Saas zone (Piemontese zone) at Lago di Cignana, Valtournanche, Italy. Compagnoni, R., Messiga, B., eds., High Pressure Metamorphism in the Western Alps: 16th IMA Meeting. Guide Book to Field Excursion, B1, p. 117-126.

Roda, M., Marotta, A.M., and Spalla, M.I., 2010, Numerical simulations of an ocean-continent convergent system: influence of subduction geometry and mantle wedge hydration on crustal recycling: Geochemistry, Geophysics, Geosystems, v. 11, p. 1-21.

_____ 2011, The effects of the overriding plate thermal state on the slab dip in an ocean-continent subduction system: Comptes Rendus – Geoscience, v. 343, p. 323-330. doi: 10.1016/j.crte.2011.01.005

Roda, M., Regorda, A., Spalla, M.I., Marotta, A.M., 2019, What drives Alpine Tethys opening? Clues from the review of geological data and model predictions: Geological Journal, v. 54, p. 2646-2664.

Roda, M., Spalla, M.I., and Marotta, A.M., 2012, Integration of natural data within a numerical model of ablative subduction: a possible interpretation for the Alpine dynamics of the Austroalpine crust: Journal of Metamorphic Geology, v. 30, p. 973-996.

Rubatto, D., Gebauer, D., and Fanning, M., 1998, Jurassic formation and Eocene subduction of the Zermatt-Saas-Fee ophiolites: implications for the geodynamic evolution of the Central and Western Alps: Contributions to Mineralogy and Petrology, v. 132, p. 269-287.

Rüpke, L.H., and Hasenclever, J., 2017, Global rates of mantle serpentinisation and H_2 production at oceanic transform faults in 3-D geodynamic models: Geophysical Research Letters, v. 44, p. 6726-6734. doi: 10.1002/2017GL072893

Scambelluri, M., and Rampone, E., 1999, Mg-metasomatism of oceanic gabbros and its control on Ti-clinohumite formation during eclogitisation: Contributions to Mineralogy and Petrology, v. 135, p. 1-17. doi: 10.1007/s004100050494

Schmidt, M.W., and Poli, S., 1998, Experimentally based water budgets for dehydrating slabs and consequences for arc magma generation: Earth and Planetary Science Letters, v. 163, p. 361-379. doi: 10.1016/S0012-821X(98)00142-3

Smith, D.C., 1984, Coesite in clinopyroxene in the Caledonides and its implications for geodynamics. Nature, v. 310, p. 641-644.

Shen, T., Hermann, J., Zhang, L., Lü, Z., Padrón-Navarta, J.A., Xia, B., and Bader, T., 2015, UHP metamorphism documented in Ti-chondrodite-and Ti-clinohumite-bearing serpentinized ultramafic rocks from Chinese southwestern Tianshan: Journal of Petrology, v. 56, p. 1425-1458.

Skora, S., Lapen, T.J., Baumgartner, L.P., Johnson, C.M., Hellebrand, E., and Mahlen, N.J., 2009, The duration of prograde garnet crystallisation in the UHP eclogites at Lago di Cignana, Italy: Earth and Planetary Science Letters, v. 287, p. 402-411.

Skora, S., Mahlen, N.J., Johnson, C.M., Baumgartner, L.P., Lapen, T.J., Beard, B.L., and Szilvagyi, E.T., 2015, Evidence for protracted prograde metamorphism followed by rapid exhumation of the Zermatt-Saas Fee ophiolite: Journal of Metamorphic Geology, v. 33, p. 711-734. doi: 10.1111/jmg.12148

Spalla, M.I., Gosso, G., Marotta, A.M., Zucali, M., and Salvi, F., 2010, Analysis of natural tectonic systems coupled with numerical modelling of the polycyclic continental lithosphere of the Alps: International Geology Review, v. 52, p. 1268-1302.

Spalla, M.I., Lardeaux, J.M., Dal Piaz, G.V., Gosso, G., and Messiga, B., 1996, Tectonic significance of Alpine eclogites: Journal of Geodynamics, v. 21, p. 257-285.

Spalla, M.I., and Zucali M., 2004, Deformation vs. metamorphic reequilibration heterogeneities in polymetamorphic rocks: a key to infer quality P-T-d-t path: Periodico di Mineralogia, v. 73, p. 249-257.

Tartarotti, P., Festa, A., Benciolini, L., and Balestro, G., 2017, Record of Jurassic mass transport processes through the orogenic cycle: Understanding chaotic rock units in the high-pressure Zermatt-Saas ophiolite (Western Alps): Lithosphere, v. 9, p. 399-407. doi: 10.1130/L605.1

Turcotte, D.L., Schubert, G., 2002, Geodynamics (2nd ed.): Cambridge University Press, New York, 848 p.

Vernon, R.H., 2018, A practical guide to rock microstructures, second edition: Cambridge University Press, Cambridge, 432 p., doi:10.1017/9781108654609

van der Klauw, S.N.G.C., Reinecke, T., and Stöckhert, B., 1997, Exhumation of ultrahigh-pressure metamorphic oceanic crust from Lago di Cignana, Piemontese zone, western Alps: the structural record in metabasites: Lithos, v. 41, p. 79-102. doi: 10.1016/S0024-4937(97)82006-3

Weber, S., and Bucher, K., 2015, An eclogite-bearing continental tectonic slice in the Zermatt-Saas high-pressure ophiolites at Trockener Steg (Zermatt, Swiss Western Alps): Lithos, v. 232, p. 336-359. doi: 10.1016/j.lithos.2015.07.010

Weber, S., Sandmann, S., Miladinova, I., Fonseca, R.O.C., Froitzheim, N., Münker, C., and Bucher, K., 2015, Dating the initiation of Piemonte-Liguria Ocean subduction: Lu-Hf garnet chronometry of eclogites from the Theodul Glacier Unit (Zermatt-Saas zone, Switzerland): Swiss Journal of Geosciences, v. 108, p. 183-199doi: 10.1007/s00015-015-0180-5

White, R.W., Powell, R., and Holland, T.J.B., 2007, Progress relating to calculation of partial melting equilibria for metapelites: Journal of Metamorphic Geology, v. 25, p. 511-527. doi: 10.1111/j.1525-1314.2007.00711.x

Whitney, D.L., and Evans, B.W., 2010, Abbreviations for names of rock-forming minerals: American Mineralogist, v. 95, p. 185-187. doi: 10.2138/am.2010.3371

Winter, J., 2001, Principles of Igneous and Metamorphic Petrology: Prentice Hall Pearson, 712 p.

Zanoni, D., Rebay, G., Bernardoni, J., and Spalla, M.I., 2012, Using multiscale structural analysis to infer high-/ultrahigh-pressure assemblages in subducted rodingites of the Zermatt-Saas Zone at Valtournanche, Italy: Journal of the Virtual Explorer, v. 41, p. 2-30. doi: 10.3809/jvirtex.2011.00290

Zanoni, D., Rebay, G., and Spalla, M.I., 2016, Ocean floor and subduction record in the Zermatt-Saas rodingites, Valtournanche, Western Alps: Journal of Metamorphic Geology, v. 34, p. 941-961. doi: 10.1111/jmg.12215

Zeh, A., Holland, T.J.B., and Klemd, R., 2005, Phase relationships in grunerite-garnet-bearing amphibolites in the system CFMASH, with applications to metamorphic rocks from the Central Zone of the Limpopo Belt, South Africa: Journal of Metamorphic Geology, v. 23, p. 1-16. doi: 10.1111/j.1525-1314.2005.00554.x

Figure captions

Figure 1. (a) Location of the studied area in the simplified tectonic framework of the Western Alps (SL = Sesia-Lanzo Zone; PL = Periadriatic line; TP = Tertiary plutons); (b) simplified structural setting of the upper Valtournanche (redrawn after De Giusti *et al.* 2003 and Forster *et al.* 2004): CLU = Cignana Lake Unit; CZ = Combin Zone; DB = Dent Blanche Nappe; PCB = Pancherot-Cime Bianche Unit; ZSZ = Zermatt-Saas Zone. AA’ cross-section is shown in Figure 1c. The red star locates the studied area (Créton outcrops) and the red rectangle Figure 1d; (c) cross-section of UHP Cignana Lake Unit and Arolla Unit (Dent Blanche Nappe) – Combin Zone – Zermatt-Saas Zone contacts (Forster *et al.* 2004); (d) foliation trajectory map with legend of Upper Valtournanche after Luoni *et al.* (2019) and Zanoni (unpublished: original mapping at 1:5000 scale); light colours indicate interpreted lithostratigraphy.

Figure 2. Form surface maps of two outcrops from Créton, showing a quite complete lithostratigraphy and sequence of superposed fabrics (modified after Luoni *et al.* 2019). Equiareal Schmidt projections for structures are shown, with number of data in brackets.

Figure 3. Mesostructures revealing the tectonic history of the Créton serpentinites. (a) Ti-chondrodite + Ti-clinohumite vein marking D1 isoclinal fold and intersected by S2 foliation: AP1 = D1 axial plane; (b) olivine-rich layer underlying D2 tight folds in olivine-rich serpentinite; (c) magnetite layer intersected by S2 and D3 discrete shear zones in serpentinite. Coin and pencil for scale.

Figure 4. Microstructures. (a) S2 foliation in serpentinite marked by Atg2 + Mag2 + Ol2, wrapping pre-D2 Ol with Mag inclusions (BSE image); (b) S2 foliation in serpentinite marked by Atg2 + Chl2 + Cpx2 (crossed polars); (c) olivine-rich layer with pre-D2 and pre-D2-to-early-D2 Ol wrapped by S2 foliation marked by Ol2 + Atg2 + Mag2 (crossed polars); (d) Cpx porphyroclast in a Atg2 + Chl2 + Cpx2 + Mag2 matrix (crossed polars); (e) Ti-Chu + Ti-Chn rim between Ilm + Mag aggregate and pre-D2-to-early-D2 Cpx (plane polarised light); (f) Core-mantle structure with pre-

D2 Ti-Chn porphyroclast surrounded by a Ti-Chn +Ti-Chu polygonal aggregate (plane polarised light).

Figure 5. (a-b-c-d) Pre-D2-to-early-D2 grains in Ti-Chu polygonal aggregates at the rim of Ti-Chn aggregates are gradually parallelised and recrystallised into S2 in BSE image (a) and Ti map (b); (c-d) pre-D2-to-early-D2 Cpx, Ti-Chu + Ti-Chn rim, Ilm + Mag aggregate in BSE image (c) and crossed polars (d).

Figure 6: Mineral chemistry diagrams. (a) olivine; (b) humites; (c) clinopyroxene; (d) serpentine; (e) spinel. Symbols refer to rocks and colours to structural stages: blue = pre-D2; red = pre-D2-to-early-D2; green = syn-D2. Ti-humite diagram is redrawn after Luoni *et al*. (2018).

Figure 7. (a) Pre-D2 (orange area) and pre-D2-to-early-D2 PT conditions (yellow area); experimentally determined fields in Ti-rich systems (black curves, redrawn from Shen *et al.* 2015); experimental data combined with Schreinemaker analysis, representing phase relations in systems with less Ti and involving Ti-humites, Atg, Opx, Ol, and Chl (grey curves, redrawn from Shen *et al.* 2015). Green and blue lines represent temperatures calculated from pre-D2 olivine (De Hoog *et al.* 2010) with error bars. The red thick curve represents Opx-in from Figure 7b; (b-c) pseudosections calculated in the CFMASHO system for syn-D2 Ol-bearing (b) and Cpx-bearing (c) mineral assemblages; compositions (mol%) are reported at the top of each pseudosection. Dotted and dashed areas in panels a,b, and c represent syn-D2 PT conditions for Valtournanche rodingites (Zanoni *et al.* 2016) and serpentinites (Rebay *et al.* 2012) respectively; (d) Inferred P-T-d-t path of Créton serpentinites redrawn after Luoni *et al*. (2019) with age data from Rebay *et al*. (2018). Geotherms (Cloos *et al*. 1993): (1) near spreading ridge or volcanic arc; (2) normal gradient of old plate interior; (3a) cold subduction zones; (3b) warm subduction zones. Orange and yellow boxes represent pre-D2 and D2, respectively and blue field represents D3 re-equilibration.

Figure 8. Setup of the numerical model. The model domain is 1400 km wide and 710 km deep. The initial lithosphere thickness is 80 km and is defined by the 1227°C isotherm. The velocity boundary

conditions correspond to a free slip condition along the bottom of the domain and a fixed velocity along the top boundary. The vertical component of the velocity vector (Uy) is fixed at 0 cm/yr on the right boundary along the entire lithospheric thickness (80 km depth) and along the left side from 0 to 700 km depth. No slip conditions are imposed on the right and left sides of the domain from the topographic surface to the upper boundary. Plate convergence is simulated with a horizontal velocity of 3 cm/yr, and it is fixed along the bottom of the oceanic crust and at the nodes of the numerical grid and distributed along a 45°-dipping plane from the trench to a depth of 100 km. The thermal boundary conditions correspond to 0°C at the top of the domain and 1227°C at the bottom. The initial thermal configuration corresponds to an uniform purely conductive upper thermal boundary layer throughout the lithosphere (from 0 to 80 km depth and from 0°C to 1227°C) and an uniform sublithospheric temperature of 1227°C (inset). The temperatures are fixed along the left vertical sidewall, and a zero thermal flux is imposed on the right side. The materials included in the model account for the upper and lower oceanic crust, continental crust, mantle, and sticky air (see Table 5 for material parameters and rheology).

Figure 9. Results of the simulation represented by geodynamic setting (a-c) and related geotherms (b-d) after 20 (a-b) and 28 Myr (c-d) of oceanic subduction, (corresponding to 80 and 72 Ma absolute ages) and comparison with the pre-D2 PT conditions (white box), defined by isotherms and depths. (a) At 80 Ma, the pre-D2 PT conditions are matched by markers that belong to the upper oceanic crust, located within the serpentinised mantle wedge and close to the slab. (b) Geotherms extrapolated at different distances from the trench indicate that the pre-D2 PT conditions occur at a distance of 100-130 km from the trench and at ca. 80-110 km depth. (c) At 72 Ma, the pre-D2 PT conditions occur in an inner portion of the mantle wedge. (d) The location of the pre-D2 PT conditions in the subduction system is reached at a distance of 110-145 km from the trench and at ca. 80-110 km depth.

Figure 10. Results of the simulation represented by geodynamic setting (a-c) and related geotherms (b-d) after 30 (a-b), 35 (c-d), and 40 Myr (e-f) of oceanic subduction, (corresponding to 70, 65, and 60 Ma absolute ages) and comparison with the D2 PT conditions (white box), defined by isotherms and depths. At 70 Ma (a), D2 PT conditions are recorded by markers of upper oceanic crust within the mantle wedge, and they are coupled with rare markers of trench sediments and some markers of continental crust. In the younger steps (c-e), the location of D2 PT conditions moves away from the slab. The maximum distance from the trench (b-d-e) varies from 125 km at 70 Ma to 155 km at 60 Ma.

Figure 11. Results of the simulation represented by geodynamic setting at 40 Ma and comparison with the PT peak conditions of Cignana Lake Unit (white box), defined by isotherms and depths (590-630°C and 2.6-3.0 GPa). At 40 Ma, several markers of oceanic crust and trench sediments achieved the PT conditions proposed for Cignana Lake Unit.

Table captions

Table 1. Metamorphic conditions and radiometric ages of the HP-UHP peaks of Zermatt-Saas Zone (modified after Rebay *et al.* 2018). Data are localised in the underlying tectonic sketch (redrawn after Dal Piaz 1999): A = Antrona Ophiolite; DB = Dent-Blanche nappe; MR = Monte Rosa; ZS = Zermatt-Saas Zone; CO = Combin Zone; Dk = II Diorite-Kinzigitic Zone; EM = Mont Emilius, GR = Glacier-Refray; MA = Mont Avic; B = Biella pluton; Emc = Eclogitic Micaschist Complex; Gm = Gneiss Minuti Complex; GP = Gran Paradiso.

Table 2. Mineral modes and assemblages marking superposed fabrics in the different rock types.

Table 3. Compositional range of olivine, serpentine, clinopyroxene, magnetite, chlorite, amphibole, and ilmenite in atoms per formula unit, in serpentinites, pyroxenite layers, and olivine-rich layers, during different deformation stages. $X_{Mg} = Mg/(Mg+ Fe^{2+})$; $X_{Fe} = Fe^{2+}/(Mg+ Fe^{2+})$.

Table 4. EMPA mineral chemical analyses selected for calculating the bulk rock composition used in pseudosections. Al ppm content of Ol was determined by ICPMS at the CNR-IGG UOS of Pavia with a LA-ICP-MS system coupling a 266 nm Nd:YAG laser probe with a quadrupole ICP-MS (DRCe from PerkinElmer), using NIST 610, NIST 612, and BCR2 standards, and GLITTER data processing. Spot size was 40–55 mm according to the mineral sizes, laser frequency 10 Hz, acquisition was for 40–60 s preceded and followed by at least 40 s background counting.

Table 5. Material and rheological parameters used in the simulation. References: a) Ranalli and Murphy 1987; b) Afonso and Ranalli, 2004; c) Kirby 1983; d) Haenel *et al.* 1988; e) Chopra and Paterson 1981; f) Dubois and Diament 1997; Best and Christiansen 2001; g) Roda *et al.* 2011; h) Schmidt and Poli 1998; i) Gerya and Stöckhert 2005; j) Roda *et al.* 2012; k) Gerya and Yuen 2003; l) Meda *et al.* 2010.

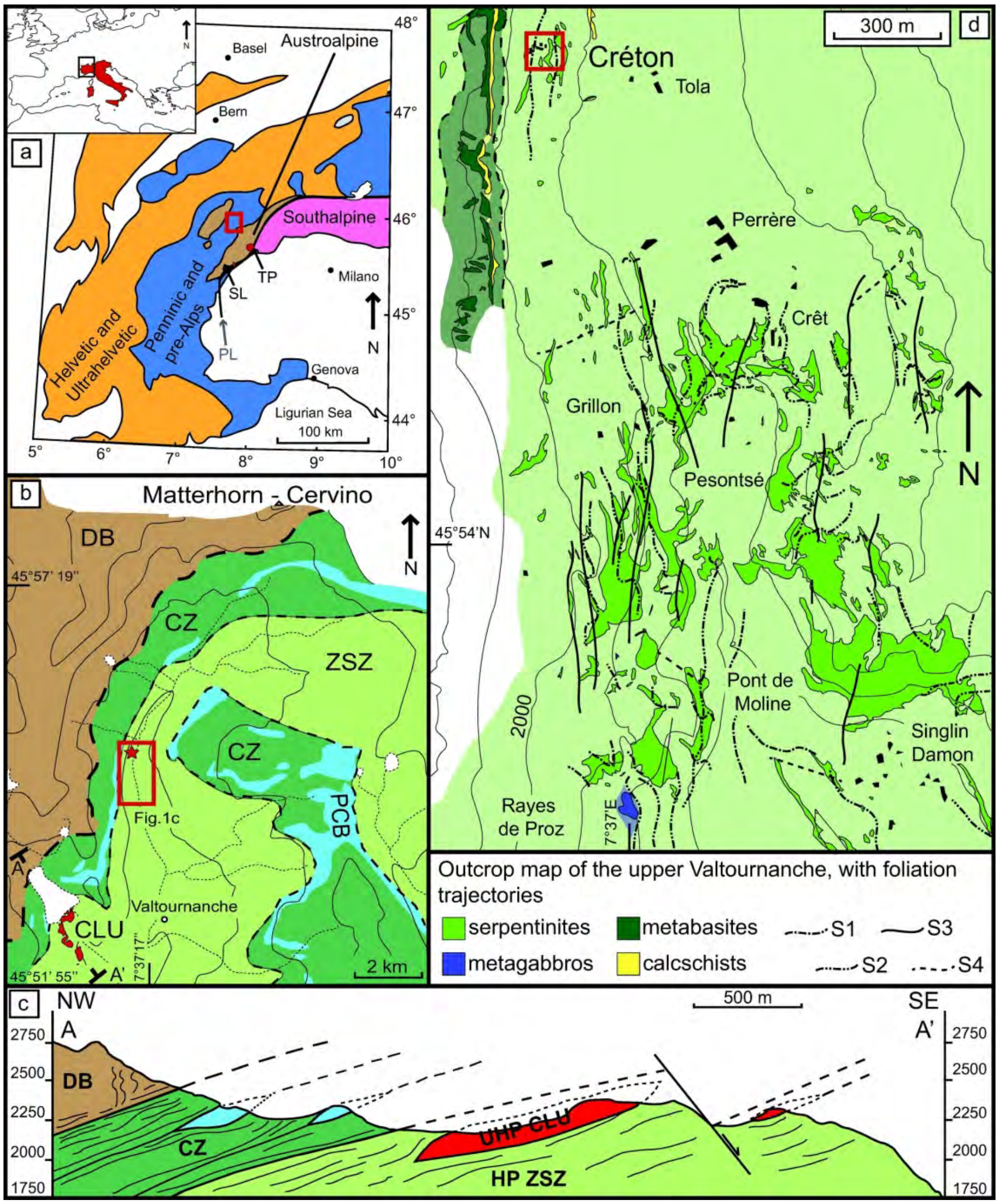

Figure 1. (a) Location of the studied area in the simplified tectonic framework of the Western Alps (SL = Sesia-Lanzo Zone; PL = Periadriatic line; TP = Tertiary plutons); (b) simplified structural setting of the upper Valtournanche (redrawn after De Giusti et al. 2003 and Forster et al. 2004): CLU = Cignana Lake Unit; CZ = Combin Zone; DB = Dent Blanche Nappe; PCB = Pancherot-Cime Bianche Unit; ZSZ = Zermatt-Saas Zone. AA' cross-section is shown in Figure 1c. The red star locates the studied area (Créton outcrops) and the red rectangle Figure 1d; (c) cross-section of UHP Cignana Lake Unit and Arolla Unit (Dent Blanche Nappe) – Combin Zone – Zermatt-Saas Zone contacts (Forster et al. 2004); (d) foliation trajectory map with legend of Upper Valtournanche after Luoni et al. (2019) and Zanoni (unpublished: original mapping at 1:5000 scale); light colours indicate interpreted lithostratigraphy.

178x215mm (300 x 300 DPI)

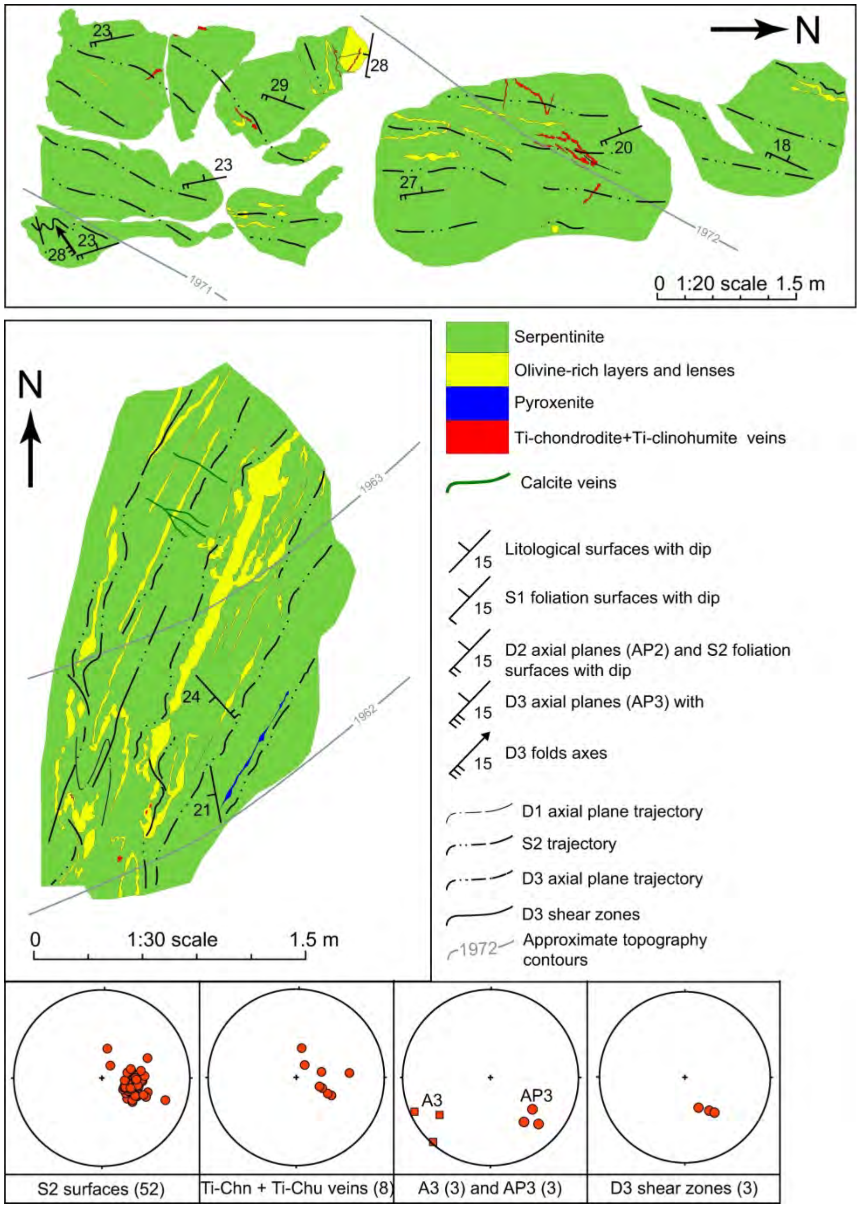

Figure 2. Form surface maps of two outcrops from Créton, showing a quite complete lithostratigraphy and sequence of superposed fabrics (modified after Luoni et al. 2019). Equiareal Schmidt projections for structures are shown, with number of data in brackets.

208x292mm (300 x 300 DPI)

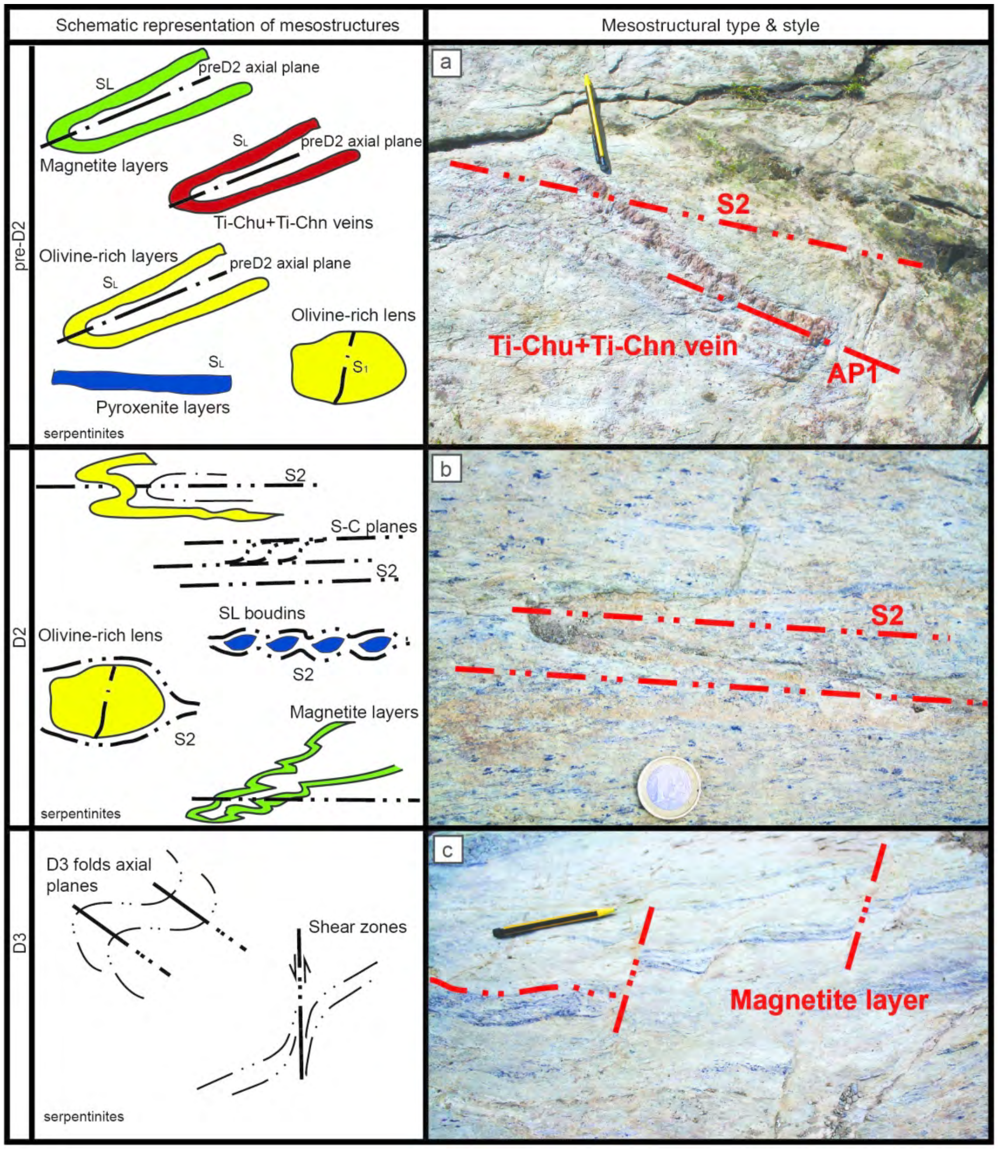

Figure 3. Mesostructures revealing the tectonic history of the Créton serpentinites. (a) Ti-chondrodite + Ti-clinohumite vein marking D1 isoclinal fold and intersected by S2 foliation: AP1 = D1 axial plane; (b) olivine-rich layer underlying D2 tight folds in olivine-rich serpentinite; (c) magnetite layer intersected by S2 and D3 discrete shear zones in serpentinite. Coin and pencil for scale.

180x206mm (300 x 300 DPI)

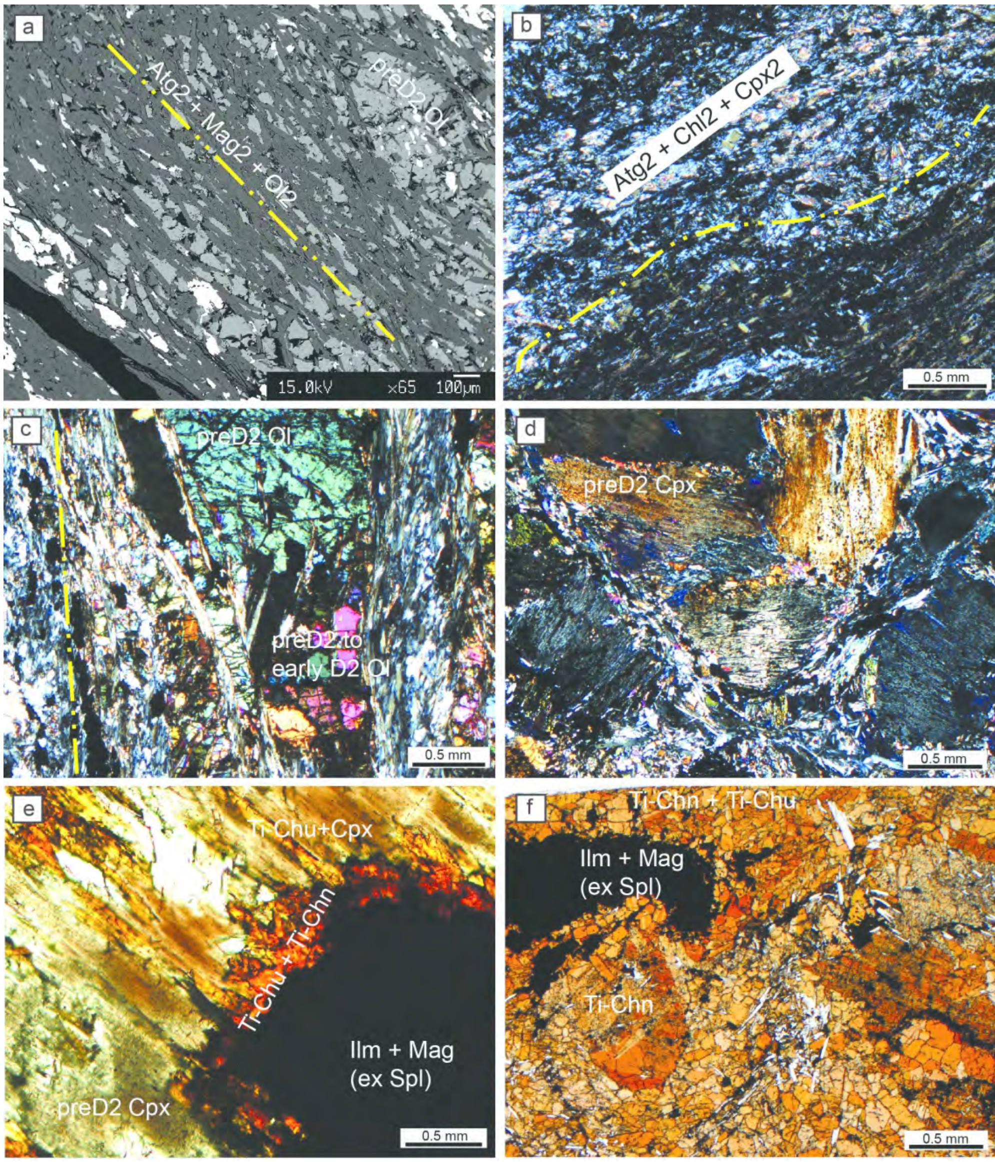

Figure 4. Microstructures. (a) S2 foliation in serpentinite marked by Atg2 + Mag2 + Ol2, wrapping pre-D2 Ol with Mag inclusions (BSE image); (b) S2 foliation in serpentinite marked by Atg2 + Chl2 + Cpx2 (crossed polars); (c) olivine-rich layer with pre-D2 and pre-D2-to-early-D2 Ol wrapped by S2 foliation marked by Ol2 + Atg2 + Mag2 (crossed polars); (d) Cpx porphyroclast in a Atg2 + Chl2 + Cpx2 + Mag2 matrix (crossed polars); (e) Ti-Chu + Ti-Chn rim between Ilm + Mag aggregate and pre-D2-to-early-D2 Cpx (plane polarised light); (f) Core-mantle structure with pre-D2 Ti-Chn porphyroclast surrounded by a Ti-Chn +Ti-Chu polygonal aggregate (plane polarised light).

178x206mm (300 x 300 DPI)

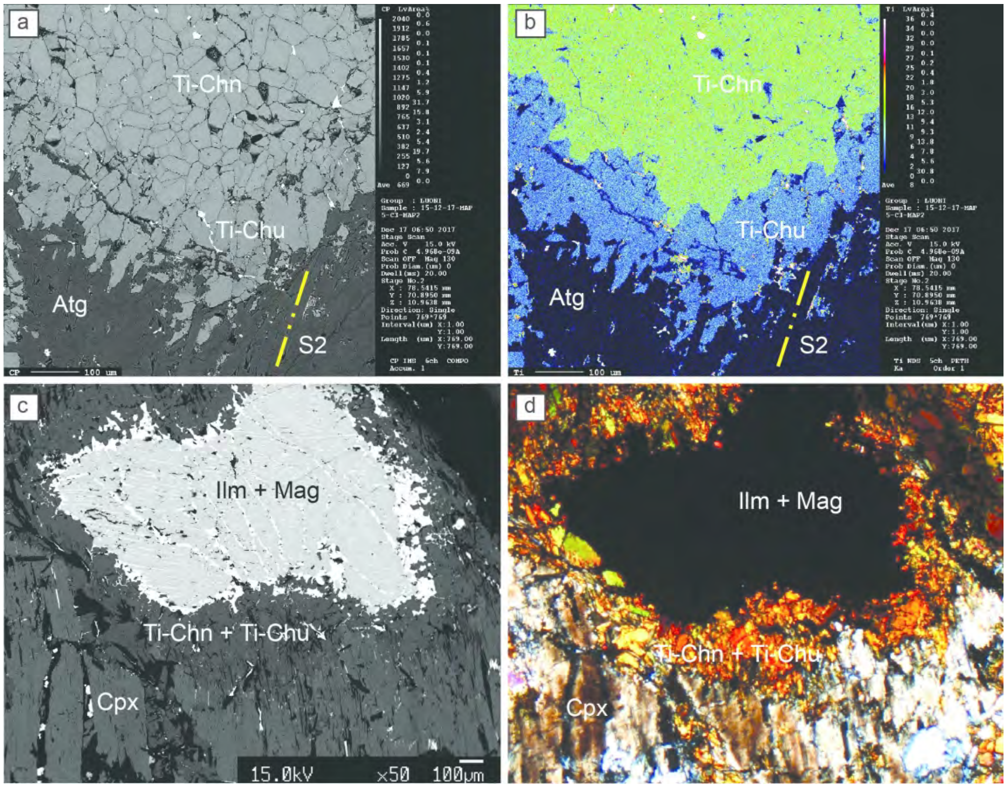

Figure 5. (a-b-c-d) Pre-D2-to-early-D2 grains in Ti-Chu polygonal aggregates at the rim of Ti-Chn aggregates are gradually parallelised and recrystallised into S2 in BSE image (a) and Ti map (b); (c-d) pre-D2-to-early-D2 Cpx, Ti-Chu + Ti-Chn rim, Ilm + Mag aggregate in BSE image (c) and crossed polars (d).

199x155mm (300 x 300 DPI)

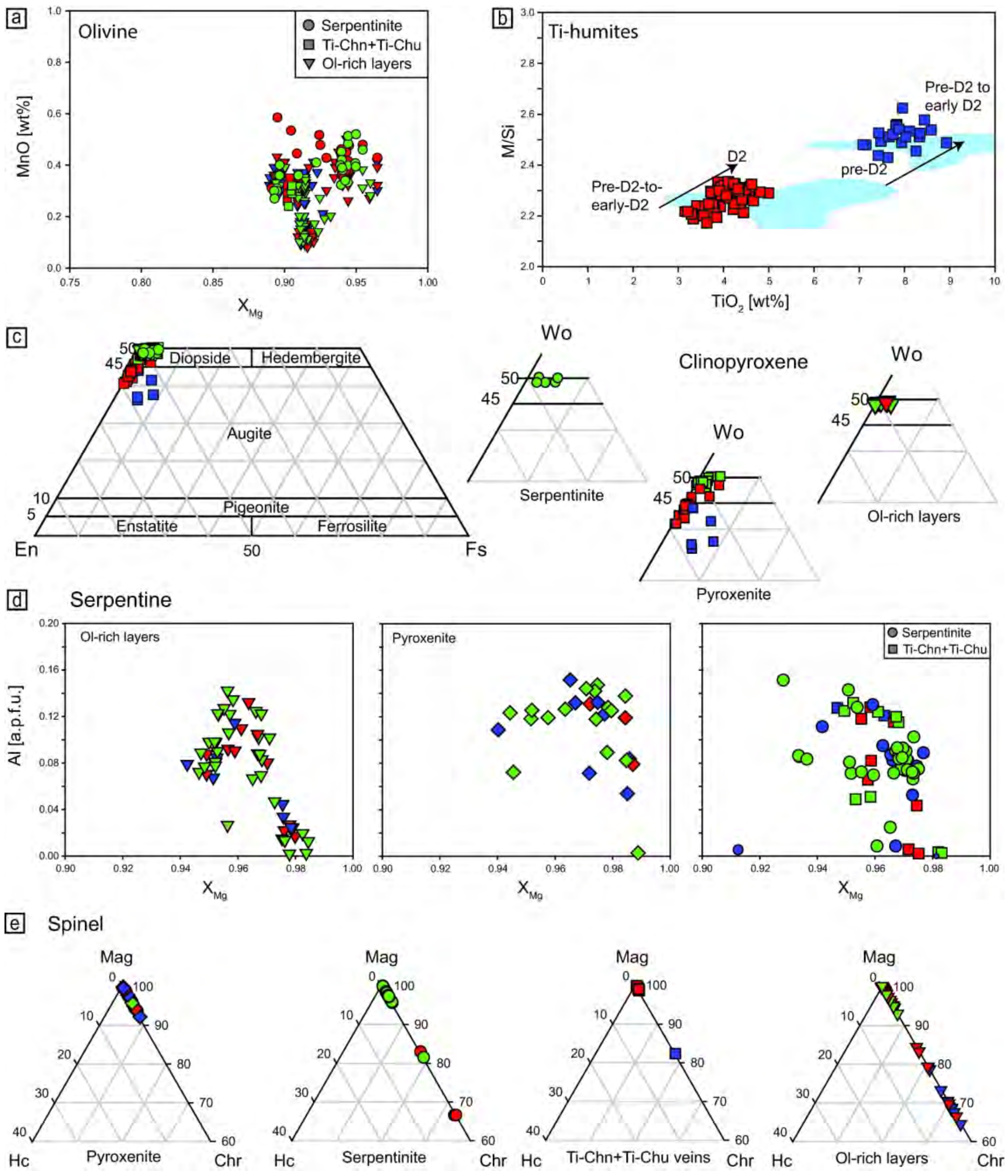

Figure 6: Mineral chemistry diagrams. (a) olivine; (b) humites; (c) clinopyroxene; (d) serpentine; (e) spinel. Symbols refer to rocks and colours to structural stages: blue = pre-D2; red = pre-D2-to-early-D2; green = syn-D2. Ti-humite diagram is redrawn after Luoni et al. (2018).

208x242mm (300 x 300 DPI)

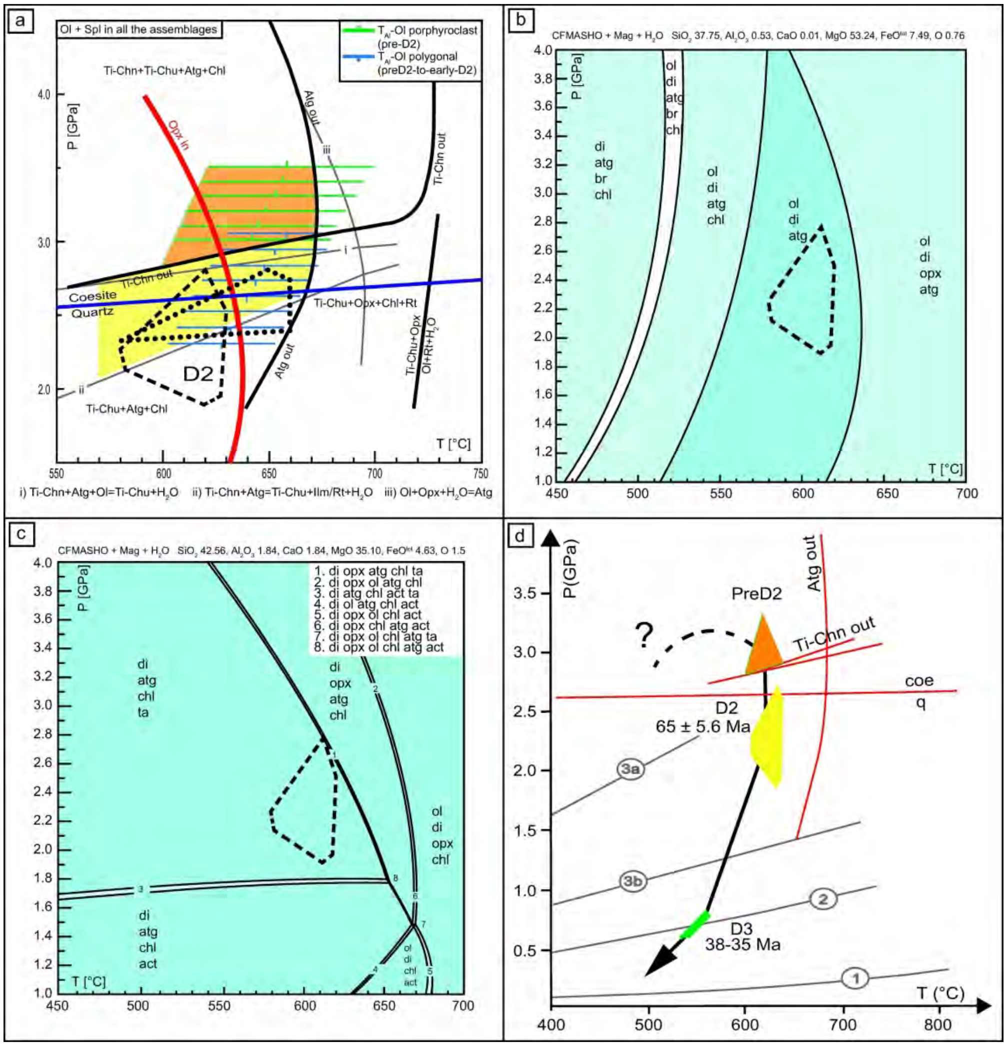

Figure 7. (a) Pre-D2 (orange area) and pre-D2-to-early-D2 PT conditions (yellow area); experimentally determined fields in Ti-rich systems (black curves, redrawn from Shen et al. 2015); experimental data combined with Schreinemaker analysis, representing phase relations in systems with less Ti and involving Ti-humites, Atg, Opx, Ol, and Chl (grey curves, redrawn from Shen et al. 2015). Green and blue lines represent temperatures calculated from pre-D2 olivine (De Hoog et al. 2010) with error bars. The red thick curve represents Opx-in from Figure 7b; (b-c) pseudosections calculated in the CFMASHO system for syn-D2 Ol-bearing (b) and Cpx-bearing (c) mineral assemblages; compositions (mol%) are reported at the top of each pseudosection. Dotted and dashed areas in panels a,b, and c represent syn-D2 PT conditions for Valtournanche rodingites (Zanoni et al. 2016) and serpentinites (Rebay et al. 2012) respectively; (d) Inferred P-T-d-t path of Créton serpentinites redrawn after Luoni et al. (2019) with age data from Rebay et al. (2018). Geotherms (Cloos et al. 1993): (1) near spreading ridge or volcanic arc; (2) normal gradient of old plate interior; (3a) cold subduction zones; (3b) warm subduction zones. Orange and yellow boxes represent pre-D2 and D2, respectively and blue field represents D3 re-equilibration.

210x218mm (300 x 300 DPI)

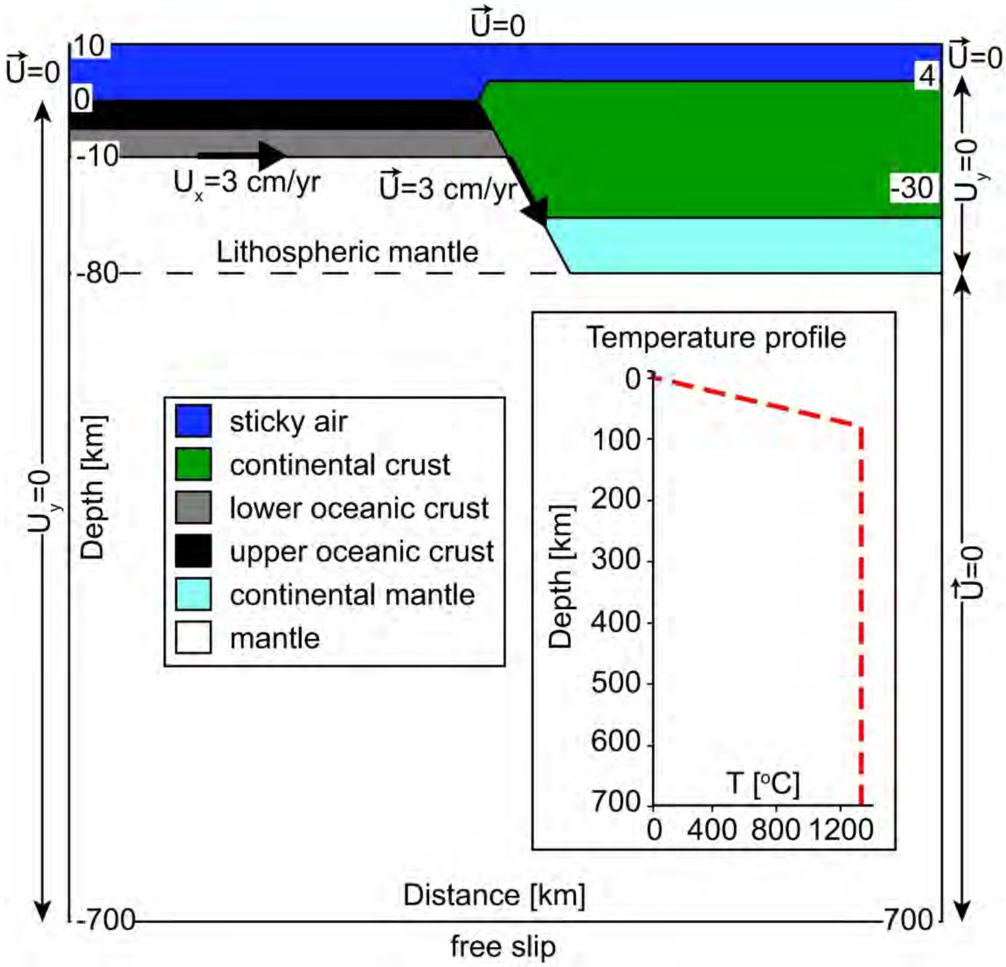

Figure 8. Setup of the numerical model. The model domain is 1400 km wide and 710 km deep. The initial lithosphere thickness is 80 km and is defined by the 1227°C isotherm. The velocity boundary conditions correspond to a free slip condition along the bottom of the domain and a fixed velocity along the top boundary. The vertical component of the velocity vector (Uy) is fixed at 0 cm/yr on the right boundary along the entire lithospheric thickness (80 km depth) and along the left side from 0 to 700 km depth. No slip conditions are imposed on the right and left sides of the domain from the topographic surface to the upper boundary. Plate convergence is simulated with a horizontal velocity of 3 cm/yr, and it is fixed along the bottom of the oceanic crust and at the nodes of the numerical grid and distributed along a 45°-dipping plane from the trench to a depth of 100 km. The thermal boundary conditions correspond to 0°C at the top of the domain and 1227°C at the bottom. The initial thermal configuration corresponds to an uniform purely conductive upper thermal boundary layer throughout the lithosphere (from 0 to 80 km depth and from 0°C to 1227°C) and an uniform sublithospheric temperature of 1227°C (inset). The temperatures are fixed along the left vertical sidewall, and a zero thermal flux is imposed on the right side. The materials included in the model account for the upper and lower oceanic crust, continental crust, mantle, and sticky air (see Table 5 for material parameters and rheology).

162x156mm (300 x 300 DPI)

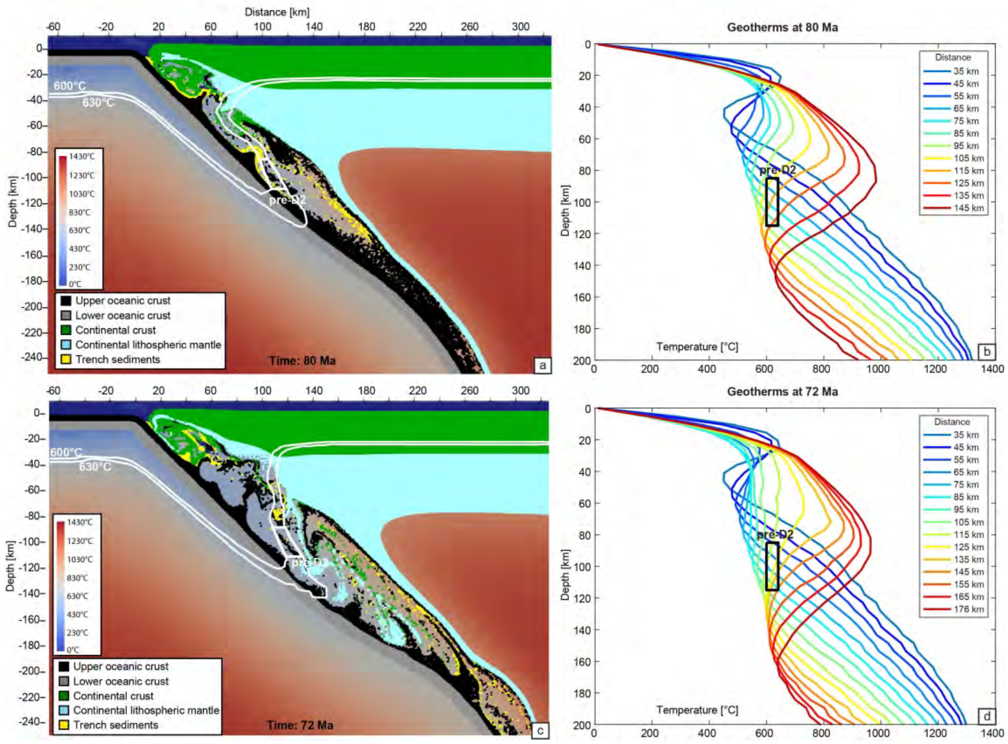

Figure 9. Results of the simulation represented by geodynamic setting (a-c) and related geotherms (b-d) after 20 (a-b) and 28 Myr (c-d) of oceanic subduction, (corresponding to 80 and 72 Ma absolute ages) and comparison with the pre-D2 PT conditions (white box), defined by isotherms and depths. (a) At 80 Ma, the pre-D2 PT conditions are matched by markers that belong to the upper oceanic crust, located within the serpentinised mantle wedge and close to the slab. (b) Geotherms extrapolated at different distances from the trench indicate that the pre-D2 PT conditions occur at a distance of 100-130 km from the trench and at ca. 80-110 km depth. (c) At 72 Ma, the pre-D2 PT conditions occur in an inner portion of the mantle wedge. (d) The location of the pre-D2 PT conditions in the subduction system is reached at a distance of 110-145 km from the trench and at ca. 80-110 km depth.

265x196mm (300 x 300 DPI)

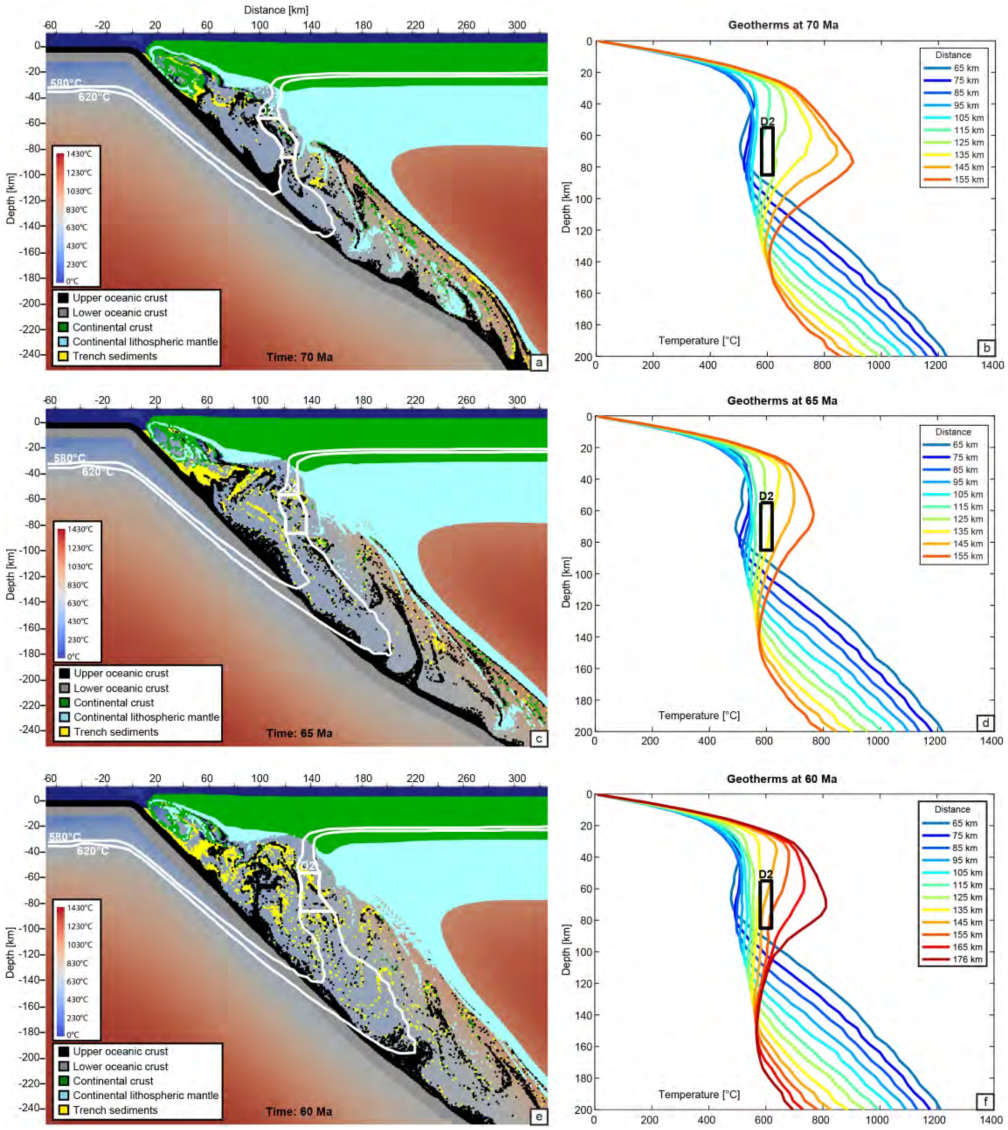

Figure 10. Results of the simulation represented by geodynamic setting (a-c) and related geotherms (b-d) after 30 (a-b), 35 (c-d), and 40 Myr (e-f) of oceanic subduction, (corresponding to 70, 65, and 60 Ma absolute ages) and comparison with the D2 PT conditions (white box), defined by isotherms and depths. At 70 Ma (a), D2 PT conditions are recorded by markers of upper oceanic crust within the mantle wedge, and they are coupled with rare markers of trench sediments and some markers of continental crust. In the younger steps (c-e), the location of D2 PT conditions moves away from the slab. The maximum distance from the trench (b-d-e) varies from 125 km at 70 Ma to 155 km at 60 Ma.

205x231mm (300 x 300 DPI)

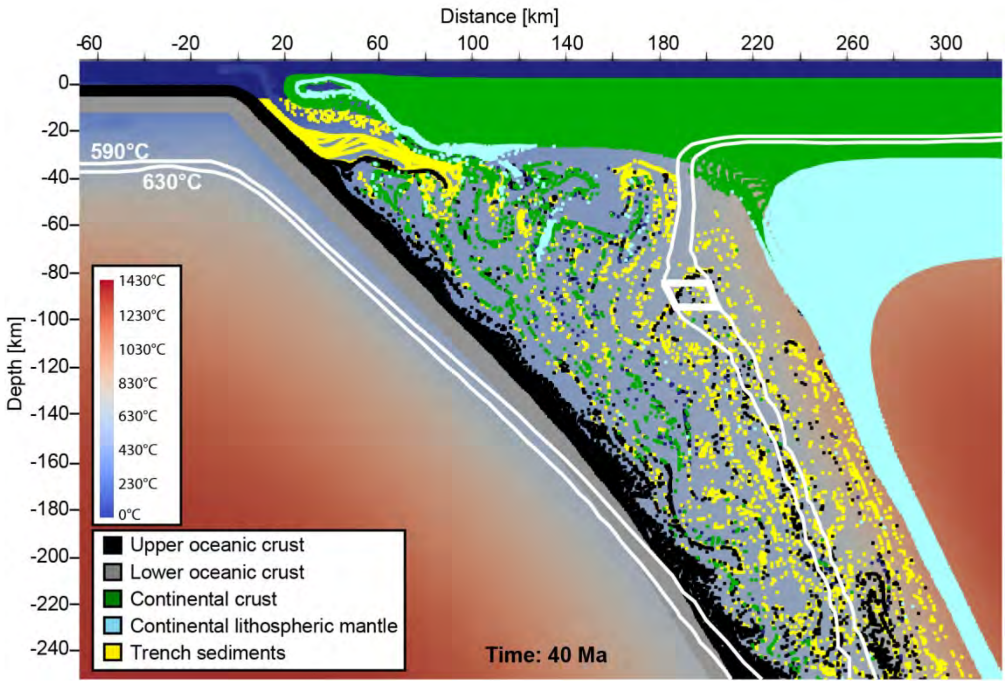

Figure 11. Results of the simulation represented by geodynamic setting at 40 Ma and comparison with the PT peak conditions of Cignana Lake Unit (white box), defined by isotherms and depths (590-630°C and 2.6-3.0 GPa). At 40 Ma, several markers of oceanic crust and trench sediments achieved the PT conditions proposed for Cignana Lake Unit.

145x98mm (300 x 300 DPI)

Key	Locality	Age (Ma)	Peak P-T conditions	Reference
1	Saas Fee	38.1 ± 2.7 - 40.7 ± 1.8		Skora *et al.* 2015
	Saas Fee		2.5 GPa 650 °C	Meyer 1983
	Saas Fee		2.5 GPa 650 °C	Bucher and Frey 1994
	Saas Fee	39.5 ± 0.1		Skora *et al.* 2015
2	Allalinhorn		1.5 GPa 570-700 °C	Chinner and Dixon 1973
	Allalinhorn		2.5 GPa 610 °C	Bucher and Grapes 2009
	Allalinhorn		2.3-2.5 GPa 530-555 °C	Angiboust *et al.* 2009
3	Mellichen	48.8 ± 2.9		Rubatto *et al.* 1998
	Mellichen	40.3 ± 9.2		Rubatto *et al.* 1998
	Mellichen		2.5-3.0 GPa 550-600 °C	Bucher *et al.* 2005
5	Pfulwe	48.9 ± 4.8	1.75-2.0 GPa 550-600 °C	Mahlen *et al.* 2006; Barnicoat and Fry 1986
	Pfulwe		2.5-3.0 GPa 550-600 °C	Bucher *et al.* 2005
6	Zermatt		1.4 GPa 600 °C	Oberhänsli 1980
	Zermatt		1.75-2.0 GPa 550-600 °C	Barnicoat 1988
7	Lichenbretter		2.0-2.5 GPa 600-650 °C	Li *et al.* 2004
	Riffelhorn-Gornergrat		2.0-2.5 GPa 600-650 °C	Li *et al.* 2004
8	Trockener Steg		2.2-2.3 GPa 515-645 °C	Weber and Bucher 2015
	Trockener Steg		2.2-2.3 GPa 450-550 °C	Weber and Bucher 2015
9	Breuil		0.8-1.2 GPa 420-520 °C	Ernst and Dal Piaz 1978
10	Valtournenche	65.5 ± 5.6	2.2-2.8 GPa 600 °C	Rebay *et al.* 2012; Rebay et al. 2018
	Valtournenche		2.3–2.8 GPa 580–660 °C	Zanoni *et al.* 2016
11	Cignana	40.6 ± 2.6	2.6-3.0 GPa ca. 600 °C	Amato *et al.* 1999; van der Klauw *et al.* 1997
	Cignana	52 ± 18 Ma		Bowtell *et al.* 1994
	Cignana	44.1 ± 0.7		Rubatto *et al.* 1998
	Cignana	44.1 ± 0.7	2.7-3.0 GPa 600 °C	Rubatto *et al.* 1998; Reinecke 1995, 1997
	Cignana	43.2 ± 1.1 - 44.4 ± 1.5		Gouzo *et al.* 2006; Reinecke 1991
	Cignana	40.7 ± 0.1	2.6-2.8 GPa 590-630 °C	Skora *et al.* 2015; Reinecke 1991
12	St. Jacques	39.2 ± 1.6	0.8-1.2 GPa 420-520 °C	Skora *et al.* 2015, Ernst and Dal Piaz 1978

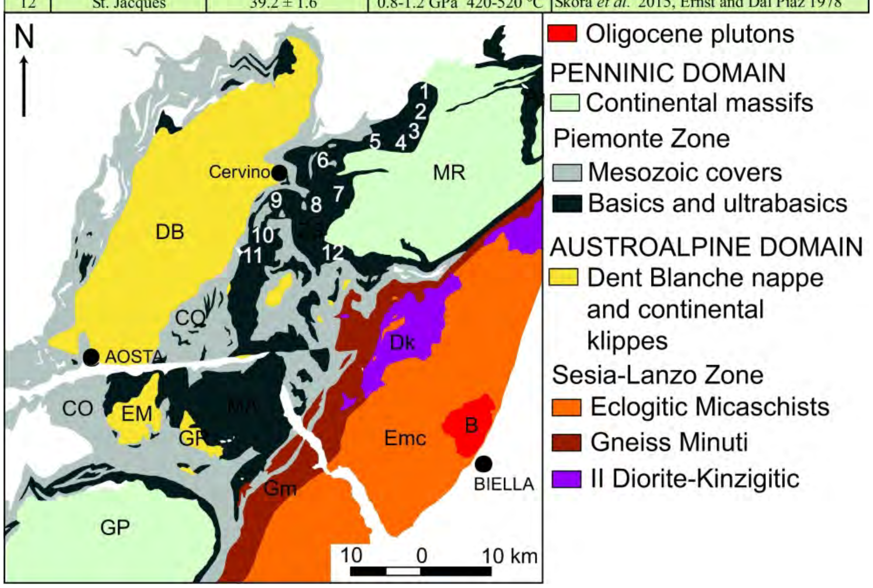

Table 1. Metamorphic conditions and radiometric ages of the HP-UHP peaks of Zermatt-Saas Zone (modified after Rebay et al. 2018). Data are localised in the underlying tectonic sketch (redrawn after Dal Piaz 1999): A = Antrona Ophiolite; DB = Dent-Blanche nappe; MR = Monte Rosa; ZS = Zermatt-Saas Zone; CO = Combin Zone; Dk = II Diorite-Kinzigitic Zone; EM = Mont Emilius, GR = Glacier-Refray; MA = Mont Avic; B = Biella pluton; Emc = Eclogitic Micaschist Complex; Gm = Gneiss Minuti Complex; GP = Gran Paradiso.

210x290mm (300 x 300 DPI)

Rock type	Mineral modes	Mineral assemblages synkinematic with successive deformation stages			
		pre-D2	pre-D2 to early D2	D2	D3 and post D2
Serpentinite	Srp (60-90%), Ol (5-30%)/Cpx (5-10%), Mag (5-15%), Ti-Chu (5%), Cal + Dol (<5%). Locally Chl, Ap (<5%)	Srp + Mag + Cpx/Ol + Ti-Chu + Dol + Ap		Srp + Mag + Cpx / Ol + Ti-Chu ± Chl ± Cal ± Dol	Srp + Mag + Chl + Cal
Ti-Chn + Ti-Chu veins	Ti-Chn + Ti-Chu (70-80%), Ol (10-20%), Atg (5-10%), Mag ± Ilm (5-10%), Chl (<5%)	Ti-Chn + Ex-Spl + Ol ± Chl + Srp	Ti-Chn + Ti-Chu + Ol + Ilm + Mag + Chl + Srp	Ti-Chu + Srp + Ol + Chl + Mag	
Pyroxenite	Cpx (70-80%), Atg ± Chl (10-20%), Ilm ± Mag (5%), Ti-Chn + Ti-Chn (5%), Amph (<2%)	Cpx (augitic core) + Spl + Srp + Chl (+ Ti-Chn)	Cpx + Srp + Chl + Ti-Chn + Ti-Chu + Ilm + Mag	Cpx + Srp + Ti-Chu + Chl + Mag	Srp + Chl + Mag + Amph
Olivine-rich layers and lenses	Ol (60-90%), Atg (10-20%), Mag ± Cr-Mag (10%), Chl (<5%), Ti-Chn + Ti-Chn (<5%), Dol (<2%) Cpx (<1%)	Ol + Srp + Mag + Cr-Mag + Cpx ± Ti-Chn + Chl	Ol + Srp + Mag + Ti-Chu + Dol	Ol + Srp + Mag + Ti-Chu	Srp + Cal

	Serpentinites				Pyroxenites				Olivine-rich layers			Olivine-rich lens
	preD2	preD2 to early D2	D2	D3	preD2	preD2 to early D2	D2	D3	preD2	preD2 to early D2	D2	
Olivine												
Fe_{tot}	0.07-0.22		0.09-0.23	-	-	-	-	-	0.07-0.23	0.07-0.22	0.08-0.22	0.14-0.18
Mg	1.79-1.92		1.81-1.90	-	-	-	-	-	1.77-1.92	1.78-1.92	1.780-1.92	1.81-1.87
Mn	0.01		0.00-0.01	-	-	-	-	-	0.01	0.01	0.01	-
X_{Mg}	0.89-0.96		0.89-0.95	-	-	-	-	-	0.89-0.96	0.89-0.96	0.89-0.96	0.90-0.93
Serpentine												
Mg	2.53-2.78	2.76-2.83	2.54-3.16	2.65-2.75	2.54-2.76	2.63-2.75	2.56-2.77	2.66-2.70	2.52-2.78	2.55-2.78	2.50-2.79	2.64-3.39
Fe_{tot}	0.05-0.24	0.07-0.12	0.04-0.39	0.09-0.14	0.09-0.22	0.09-0.14	0.09-0.21	0.10-0.16	0.06-0.16	0.06-0.14	0.05-0.14	0.04-0.20
Al	0.00-0.13	0.0-0.07	0.0-0.15	0.03-0.13	0.05-0.15	0.03-0.13	0.0-0.15	0.10-0.15	0.01-0.11	0.02-0.13	0.0-0.14	0.0-0.13
Clinopyroxene												
Fe^{2+}	-	-	0.0-0.05	-	0.02-0.13	0.0-0.7	0.0-0.06	-	0.03	0.03	-	0.03
Fe^{3+}	-	-	0.0-0.09	-	0.11-0.14	0.0-0.14	0.0-0.08	-	-	-	-	-
Mg	-	-	0.88-1.00	-	0.91-1.01	0.93-1.06	0.92-1.05	-	0.97-0.98	0.96-0.98	-	0.95
Ca	-	-	0.97-1.00	-	0.73-0.87	083-0.96	0.95-1.02	-	0.97-0.98	0.97-0.98	-	1
Na	-	-	0.00-0.01	-	0.03-0.05	0.01-0.03	0.0-0.01	-	-	-	-	-
Ti	-	-	-	-	0.02-0.03	0.0-0.05	-	-	-	-	-	-
Magnetite												
Fe^{2+}	0.70-0.92	0.90-0.99	0.84-0.99	-	0.92-1.01	0.93-0.96	0.91-0.99	-	0.74-0.94	0.73-0.93	0.86-0.94	0.75-0.90
Fe^{3+}	1.28-1.98	1.88-1.98	1.-60-1.99	-	1.74-1.98	1.84-1.96	1.91-1.99	-	1.34-1.99	1.29-1.99	1.85-1.99	1.25-1.98
Cr	0.0-0.63	0.0-0.02	0.0-0.06	-	0.0-0.15	0.02-0.11	0.0-0.11	-	0.0-0.62	0.0-0.65	0.0-0.14	0.01-0.68
Chlorite												
Fe_{tot}	0.56-0.68	0.52-0.67	0.55-0.88	-	0.58-0.91	0.57-0.63	0.53-0.94	-	-	-	-	0.47-0.71
Mg	9.74-10.04	9.84-10.04	9.69-10.08	-	9.51-9.91	9.86-9.91	9.57-10.01	-	-	-	-	9.70-10.02
Al	2.43-2.85	2.52-2.99	2.70-3.13	-	2.59-2.99	2.75-2.96	2.53-3.02	-	-	-	-	2.41-2.97
Ilmenite												
Fe^{2+}	-	0.59-0.85	0.39-0.67	-	-	0.35-0.61	0.6	-	-	-	-	-
Fe^{3+}	-	0.03-0.07	0.03-0.08	-	-	0.01-0.04	0.02-0.03	-	-	-	-	-
Ti	-	0.96-0.98	0.96-0.98	-	-	0.98-0.99	0.98-0.98	-	-	-	-	-

Clinopyroxene					
Rock	Pirossenite			Serpentinite	Dunite
Texture	Pre-D2	Pre-D2-to-D2	D2	D2	Pre-D2
SiO_2	50.62	51.04	54.15	52.15	55.81
TiO_2	1.25	0.48	0.03	0.00	0.00
Al_2O_3	1.96	3.12	0.00	0.33	0.02
Cr_2O_3	0.03	0.81	0.00	0.00	0.00
FeO_t	8.67	2.80	0.90	4.39	1.10
MnO	0.37	0.13	0.00	0.59	0.03
MgO	16.57	17.18	18.20	15.82	18.02
CaO	18.87	22.40	24.92	24.71	24.89
Na_2O	0.71	0.28	0.00	0.05	0.01
K_2O	0.00	0.00	0.00	0.00	0.01
NiO	0.04	0.01	0.05	0.14	0.02
Sum	100.65	100.16	100.40	100.18	99.91
6 Ox					
Si	1.88	1.88	1.99	1.95	2.023
Ti	0.03	0.01	0.00	0.00	0.000
Al^{IV}	0.09	0.12	0.00	0.01	0.000
Al^{VI}	0.00	0.02	0.00	0.00	0.001
Cr	0.00	0.02	0.00	0.00	0.000
Fe^{2+}	0.13	0.02	0.01	0.05	0.033
Fe^{3+}	0.14	0.06	0.02	0.09	0.000
Mn	0.01	0.00	0.00	0.02	0.001
Mg	0.92	0.95	1.00	0.88	0.973
Ca	0.75	0.89	0.98	0.99	0.967
Na	0.05	0.02	0.00	0.00	0.001
K	0.00	0.00	0.00	0.00	0.000
Ni	0.00	0.00	0.00	0.00	0.001
Sum	4.00	4.00	4.00	4.00	4.00

Olivine					
Rock	Ti-humite veins		Ol-rich layers		
Texture	Pre2	Pre-D2-to-D2	Pre-D2-to-D2	Pre-D2-to-D2	D2
SiO_2	39.73	40.06	40.99	40.89	41.97
TiO_2	0.00	0.01	0.08	0.02	0.00
Al_2O_3	0.02	0.13	0.01	0.04	0.00
Cr_2O_3	0.02	0.11	0.06	0.01	0.00
FeO_t	9.75	9.52	8.55	8.80	4.57
MnO	0.29	0.34	0.33	0.33	0.31
MgO	50.37	50.17	49.87	49.76	52.88
CaO	0.00	0.02	0.00	0.01	0.01
Na_2O	0.00	0.00	0.03	0.00	0.00
K_2O	0.00	0.03	0.00	0.00	0.00
NiO	0.08	0.16	0.06	0.13	0.16
Sum	100.26	100.55	99.98	99.99	99.90
4 Ox					
Si	0.97	0.98	1.00	1.00	1.01
Ti	0.00	0.00	0.00	0.00	0.00
Al	0.00	0.00	0.00	0.00	0.00
Cr	0.00	0.00	0.00	0.00	0.00
Fe^{2+}	0.20	0.19	0.17	0.18	0.09
Mn	0.01	0.01	0.01	0.01	0.01
Mg	1.84	1.83	1.81	1.81	1.89
Ca	0.00	0.00	0.00	0.00	0.00
Na	0.00	0.00	0.00	0.00	0.00
K	0.00	0.00	0.00	0.00	0.00
Ni	0.00	0.00	0.00	0.00	0.00
Sum	3.03	3.02	3.00	3.00	2.99
Al (ppm)	0.33-3.59	0.88-2.05			

	Ti-clinohumite		Ti-chondrodite		Amphibole
Rock	Ti-chn + Ti-Chu veins		Ti-chn + Ti-Chu veins		Serpentinite
Texture	Pre-D2-to-D2	D2	Pre-D2	Pre-D2 to D2	Post-D2
SiO_2	36.78	37.14	32.80	32.81	58.18
TiO_2	4.14	3.68	7.93	9.22	0.04
Al_2O_3	0.00	0.01	0.02	0.02	0.07
Cr_2O_3	0.00	0.04	0.00	0.00	0.00
FeO_t	9.21	9.27	9.86	9.69	2.02
MnO	0.28	0.33	0.34	0.40	0.11
MgO	48.67	48.42	46.08	45.56	23.21
CaO	0.01	0.01	0.06	0.00	13.30
Na_2O	0.00	0.01	1.30	0.03	0.10
K_2O	0.01	0.01	0.14	0.00	0.01
NiO	0.04	0.11	0.14	0.05	0.02
Sum	99.14	99.04	98.67	97.77	99.26
	13 cations		7 cations		23 oxygens
Si	3.97	4.01	1.93	1.98	8.00
Ti	0.34	0.30	0.35	0.42	0.00
Al	0.00	0.00	0.00	0.00	0.01
Cr	0.00	0.00	0.00	0.00	0.00
Fe^{2+}	0.83	0.84	0.49	0.49	0.23
Mn	0.03	0.03	0.02	0.02	0.01
Mg	7.83	7.80	4.04	4.09	4.76
Ca	0.00	0.00	0.00	0.00	1.96
Na	0.00	0.00	0.15	0.00	0.02
K	0.00	0.00	0.01	0.00	0.00
Ni	0.00	0.01	0.01	0.00	
Sum	13.00	13.00	7	7	14.99

	Continental crust	Upper oceanic crust	Lower oceanic crust	Dry mantle	Serpentinised mantle	Sediments	Sticky air
Rheology	Dry granite		Diabase	Dry dunite	Serpentinite		
μ_0 (Pa s)	3.47E+21	1.61E+19	1.61E+22	5.01E+20	1.00E+19	1.00E+19	1.00E+19
ρ_0 (kg m^{-3})	2640	2961	2961	3200	3000	2640	1000
K (W m^{-1} K^{-1})	3.03	2.1	2.1	4.15	4.15	3.03	0.026
H_r (μW m^{-3})	2.5	0.4	0.4	0.002	0.002	2	-
E (kJ mol^{-1})	38.43	103	103	130			
References	a,d,f,l	b,f,j,k,l	a,b,c,f,l	c,d,e,f,j,l	d,f,g,h,i	g,j	g,j